AMERICAN UNIVERSITY OF BEIRUT

OPTIMIZING THE DESIGN OF A BARBED SUTURE FOR FLEXOR TENDON REPAIR USING EXTENDED FINITE ELEMENT ANALYSIS

by
HIBA MOHAMAD KOBEISSI

A thesis
submitted in partial fulfillment of the requirements
for the degree of Master of Engineering
to the Department of Mechanical Engineering
of the Faculty of Engineering and Architecture
at the American University of Beirut

Beirut, Lebanon
April 2017

AMERICAN UNIVERSITY OF BEIRUT

OPTIMIZING THE DESIGN OF A BARBED SUTURE FOR FLEXOR TENDON REPAIR USING EXTENDED FINITE ELEMENT ANALYSIS

by

HIBA M. KOBEISSI

Approved by:

Dr. Elie Shammas, Assistant Professor — Advisor

Mechanical Engineering

Dr. Mu'Tasem Shehadeh, Associate Professor — Member of Committee

Mechanical Engineering

Dr. Youssef Bakhach, Assistant Professor — Member of Committee

Surgery

Date of thesis defense: April 27, 2017

AMERICAN UNIVERSITY OF BEIRUT

THESIS, DISSERTATION, PROJECT RELEASE FORM

Student Name:

_____

Last First Middle

◯ Master's Thesis ◯ Master's Project ◯ Doctoral Dissertation

☐ I authorize the American University of Beirut to: (a) reproduce hard or electronic copies of my thesis, dissertation, or project; (b) include such copies in the archives and digital repositories of the University; and (c) make freely available such copies to third parties for research or educational purposes.

☐ I authorize the American University of Beirut, to: (a) reproduce hard or electronic copies of it; (b) include such copies in the archives and digital repositories of the University; and (c) make freely available such copies to third parties for research or educational purposes after:

One ---- year from the date of submission of my thesis, dissertation, or project.

Two ---- years from the date of submission of my thesis, dissertation, or project.

Three ---- years from the date of submission of my thesis, dissertation, or project.

_____

Signature Date

ACKNOWLEDGMENTS

I would have never been able to complete the work presented in my thesis hadn't it been for the utmost guidance of my committee members, the persistent encouragement of my friends, and the boundless support of my family.

My sincere gratitude goes to my advisor and committee members, Dr. Elie Shammas and Dr. Mu'Tasem Shehadeh for their continuous mentorship, unfailing patience and sustained commitment and motivation. Thank you for the rewarding graduate school experience. I could not have asked for better advisors.

I would like to thank Dr. Youssef Bakhach for being on my thesis committee despite his demanding schedule. Your insightful input and useful feedback helped in developing my background on sutures, in general, and tendon suturing techniques in particular.

Special thanks to Dr. Samir Mustapha for always "making" the time to welcome my questions on ABAQUS and share his knowledge on using the software with me. Your advice and comments have been of great benefit. I would also like to thank Dr. Mohamad Ghassan Abiad for his help in conducting experiments and for giving me permission to use the universal testing machine.

To my fellow lab mates, thank you for being part of my enriching journey. You were always there to cheer me up when things went down.

To the dearest to my heart, my parents, sister, and two brothers, I am forever indebted to you for where I am today and where I will be in the future. Your endless love and support have never failed me.

AN ABSTRACT OF THE THESIS OF

Hiba M. Kobeissi for Master of Engineering

Major: Mechanical Engineering

Title: Optimizing the Design of a Barbed Suture for Flexor Tendon Repair Using Extended Finite Element Analysis

Conventional surgeries for flexor tendon repair involve tying the ends of the suture in at least a single knot. Knots give rise to several complications at the repair site, from delaying wound healing, to constriction of blood flow and formation of scars. In addition, they present probable failure regions due to increased stress concentrations. To strengthen such critical locations, one approach is to use multiple suture strands. However, applying higher stresses on the tendon results in stiffer tissues that have reduced gliding ability. A promising solution implements sutures with protruding barbs that anchor themselves into the tissue; eliminating the need for a knot. The use of barbed sutures for flexor tendon repair offers several advantages over traditional knotted techniques. When barbs are inserted into the tendon, grip is achieved at multiple points. Consequently, the load is dispersed along the entire length of the suture decreasing the possibility of slippage. Furthermore, since knots are no longer required, regions with increased mass and volume of suture material are eliminated; hence, inflammation is reduced and healing of the wound is accelerated.

The purpose of this study is to propose an enhanced barbed suture geometry such that it is capable of withstanding higher stresses, in an attempt to eliminate knots in tenorrhaphies and minimize the number of suture strands used. It is believed that the rigidity of the barb, as well as its ability to anchor surrounding tissue can be manipulated by the suture's geometry via three factors: cross-sectional configuration, cut angle and cut depth.

Inspired by the geometry of flexor tendons, an elliptical, rather than a circular, cross-section was investigated. The mechanical behavior of five different aspect ratios (ρ= 1/3, 1/2, 1, 2, 3), three different cut angles (150°, 154°, 160°) and three different cut depths (0.07mm, 0.12mm, 0.18mm) was studied via extended finite element analysis using ABAQUS, for two different loading conditions; one to assess the strength of the suture, the second to evaluate the strength of a single barb.

Based on the results, an elliptical suture having an aspect ratio 1/2, cut angle 160°, and cut depth 0.12mm is recommended.

CONTENTS

ILLUSTRATIONS

TABLES

CHAPTER 1

INTRODUCTION

Several techniques have been developed for flexor tendon repair using sutures. These procedures include the traditional Kessler technique, modified 2-strand Kirchmayr-Kessler technique, Pennington modified Kessler, double Pennington modified Kessler, 4-strand Savage and 6-strand Savage [1-4] (Fig.1). These conventional methods involve tying the ends of the suture in at least a single knot. In addition to delaying wound healing, constriction of blood flow, and formation of scars, suture knots present probable failure regions due to increased stress concentrations. A solution is to use multiple strands of sutures in order to increase their strength. However, increasing the magnitude of the stress applied on the tendon results in stiffer tissues that have a reduced gliding ability, forming adhesions [1, 5-7].

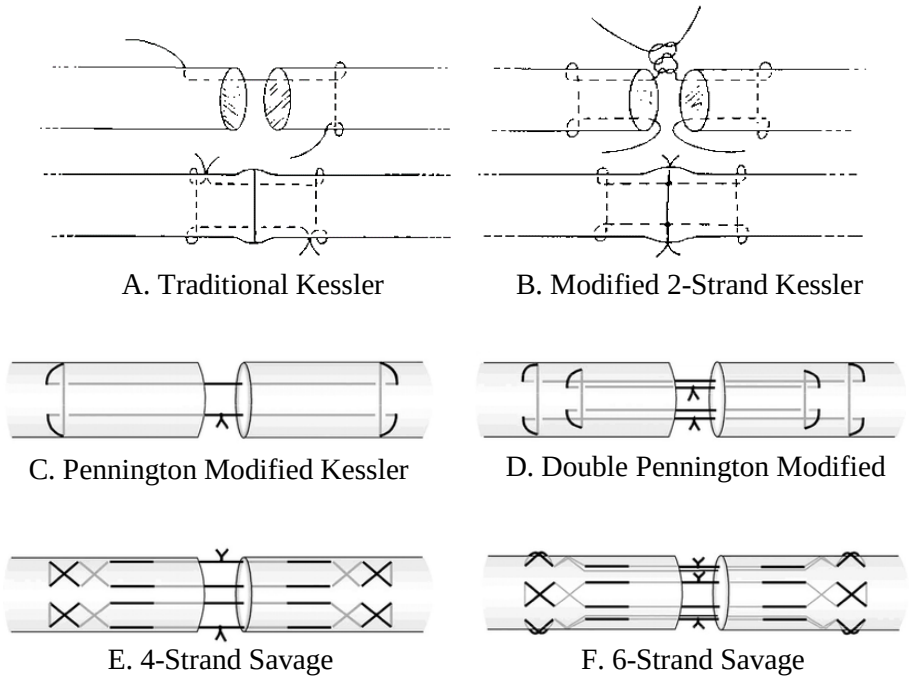

Figure 1: Different conventional knotted repair techniques [3, 8]

A promising technique that surpasses the disadvantages of the traditional tendon repair methods was first proposed by McKenzie in 1967. He developed custom-made 3-0 nylon sutures with protruding barbs that anchor themselves into the tissue (Fig. 2.A & B); hence, eliminating the need for a knot. He also demonstrated that barbed suture tenorrhaphy is capable of achieving a tensile strength comparable with that realized with a two-strand Bunnell repair with G40 stainless steel wire (17.8 – 26.7 N) [6, 9] (Fig. 2C). Furthermore, when this method was tested on canines, flexor tendons healed after 5 weeks of immobilization [9].

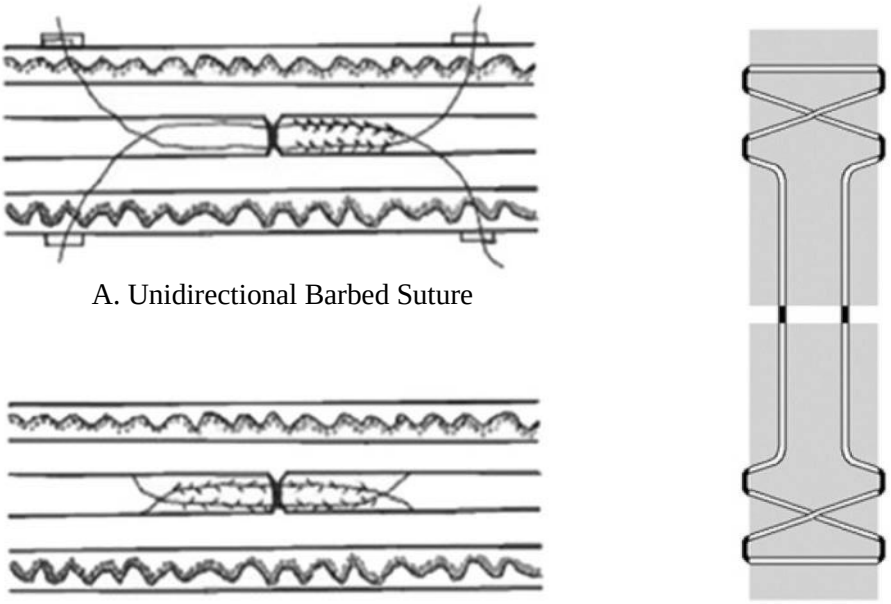

A. Unidirectional Barbed Suture

B. Bidirectional Barbed Suture

C. 2-Srand Bunnell Repair

Figure 2: A.&B. Mckenzie's suture with protruding barbs. C. Bunnell repair [5, 10]

Although little research on this novel suturing method for tendon repair has been conducted back then, its success in preliminary experimental procedures can be attributed to the following advantages. When the barbs are inserted into the tendon along the entire

length of the suture, the load is dispersed over an extended area, providing evenly distributed forces throughout the suture length [2, 11, 12]. Also, grip between the suture and the tendon is achieved at multiple points; thus, the possibility of slippage is decreased [12, 13]. Furthermore, since no knots are required, no regions with increased mass and volume of suture material are present; hence, inflammation is reduced and healing of the wound is accelerated [1, 2, 14].

Recently, the application of barbed sutures for tenorrhaphy has been of great interest. The conducted research focuses mainly on three different aspects: the mechanical properties of sutures in general and available barbed sutures in specific [4, 7, 15-18], tendon-barbed suture interaction in terms of tensile strength and suture/tissue pullout tests [4, 5, 12, 19-21], and finally, though performed less extensively, finite element modeling of barbed sutures under loading [13, 22].

The studies promote barbed sutures as a potential knotless flexor tendon repair technique. They demonstrate that knotless four strand as well as bi-directional suture repairs provide equivalent maximum tensile load, as well as 2-mm gapping at the repair site when compared with the traditional knotted techniques [1, 4, 6, 9, 11, 23]. Furthermore, a study performed using a large-diameter 0 unidirectional barbed suture showed that a four-strand Kirchmayr-Kessler procedure exhibited higher maximum tensile load and equivalent 2-mm gapping when implemented using a 0 barbed suture rather than a 3-0 braided polyester [14].

Ingle et al. suggested that tissue-specific barbed sutures need to be developed [13, 19, 20, 22]. Experiments performed on both skin and tendon indicate that the latter has a higher tensile modulus and is significantly stiffer [19]. Also, pullout test simulations

reveal shear stresses that are higher by 2 order of magnitudes for tendon versus skin tissue [22]. Hence, tendons require barbs that are more rigid as compared to skin such that they are capable of penetrating the stiffer tissue and securing the medium.

Finite element analysis of the mechanical behavior of barbed sutures imply that the rigidity of the barb, as well as its ability to anchor surrounding tissue can be manipulated by the suture's geometry via two factors: cut angle and cut depth [13, 19, 22] (Fig. 3). For a constant cut depth, an increase in cut angle results in barbs that are more flexible. On the other hand, increasing the cut depth for a constant cut angle has no significant effect on the barb's stiffness, rather it enhances the barb's ability to anchor the surrounding matrix [22]. With respect to tendons, a cut angle of 150° and a cut depth of 0.18mm were found to be most suitable based on the tensile peak load withstood [13, 19].

Figure 3: Cut depth and cut angle of a barbed suture

The failure of barbed sutures has been investigated via performing tendon/suture pullout tests. Two prominent failure modes were detected: suture pullout and peeling of

the barb [4, 12, 19-21]. However, such results have not been replicated via finite element modeling. Furthermore, the roughly elliptical nature of the flexor tendon's cross-section has not been taken into consideration when optimizing the barbed suture's geometry [13, 19, 22].

1.1. Objective

In this study, an optimized barbed suture geometry for a novel single strand flexor tendon repair procedure is designed. Finite element analysis is implemented in order to investigate the effect of varying three geometrical factors: the cross-sectional configuration, cut angle, and cut depth, on the strength of the suture. As a first step, the viscoelastic mechanical properties of the suture material, polypropylene, are determined experimentally. A failure analysis using the extended finite element analysis is then performed on ABAQUS. The performance of the various geometries is studied for two different loading conditions; one to assess the strength of the suture, the second, to evaluate the strength of a single barb. In view of the results, the possibility of using a single barbed suture for tendon repair is assessed.

CHAPTER 2

THEORETICAL BACKGROUND

2.1. Viscoelastic material

Barbed sutures, whether resorbable or not, are made from polymers that include polypropylene, polyimide, polyester, polybuster, polylactic acid, polyglyconate, and polydioxanone [7, 18, 24, 25], and exhibit viscoelastic behavior.

Viscoelastic materials retain a combination of both viscous and elastic properties. Two major models are available for describing their behavior. The first method, the integral model, is based on the Boltzmann superposition principle and defines an integral equation to represent linear viscoelasticity. According to Boltzmann's principle, the response of a specimen is affected by the entire loading history that preceded. Furthermore, subjecting a loaded material to an additional load produces a response that is exactly the same as the one that would have been induced had the total of both loads been initially applied and left to creep for the same time period. Based on this theory, a mathematical formulation is derived to describe viscoelastic behavior. In general, the total strain at any time t is expressed as [26]:

$$\varepsilon(t) = \int_{-\infty}^{t} J(t-\tau_n)d\sigma(\tau_n) \qquad \text{(Eq. 1)}$$

where $J(t-\tau_n)$ is the creep compliance.

The second method, the differential representation, models a viscoelastic behavior via a combination of Hookean springs and Newtonian dashpots, resulting in a linear differential equation. The simplest assemblage consists of a single spring and a

dashpot, where a series combination corresponds to the Maxwell model and a parallel one to the Voigt/Kelvin model (Fig. 4). For stress-relaxation experiments, the Maxwell model results in the linear differential expression for stress decay:

$$\frac{d\sigma}{\sigma} = -(E_m / \eta_m)dt \qquad \text{(Eq. 2)}$$

Integrating the above expression for the initial conditions $t = 0$ and $\sigma(t = 0) = \sigma_0$ yields the solution:

$$\sigma = \sigma_0 \exp(-t / \tau) \qquad \text{(Eq. 3)}$$

where the characteristic time constant $\tau = \eta_m / E_m$.

In a similar manner, creep experiments can be modelled using the Voigt/Kelvin model:

$$\varepsilon = \varepsilon_0 \exp(-t / \tau) \qquad \text{(Eq. 4)}$$

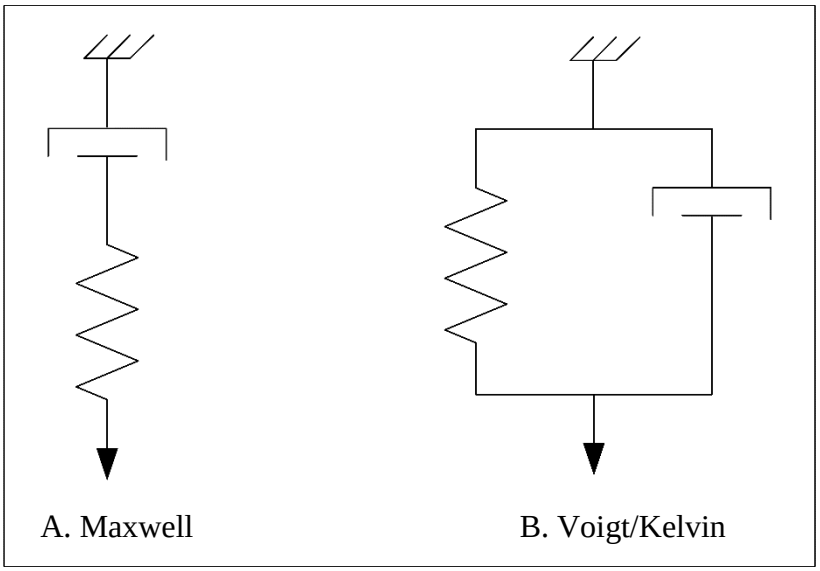

Figure 4: Differential representation of viscoelastic material: A.Maxwell and B.Voigt/Kelvin models

Creep behavior is more appropriately represented by a Voigt/Kelvin rather than a Maxwell model, for when the latter is subjected to a constant load, the dashpot will permit viscous flow, and the spring will be under constant tension. As such, only the Newtonian characteristics of the material are exhibited. However, creep experiments reveal different observations and likewise, a Maxwell model is unfitting for their description [26, 27].

On the other hand, implementing a Voigt/Kelvin model to describe stress-relaxation experiments results in an elastic behavior. In order to overcome such limitations, both models are combined into what is known as the standard linear solid model consisting of a spring in parallel with a Maxwell model. More complex models can be assembled; the most advantageous of which being the generalized Maxwell or Voigt/Kelvin models which consist of either a parallel arrangement of a spring and a number of Maxwell elements or a series combination of a spring and a number of Voigt/Kelvin elements such that a range of time characteristics is obtained (Fig. 5) [26, 27].

The generalized Maxwell and Voigt/Kelvin models allow for a mathematical representation of a linear viscoelastic behavior subjected to stress-relaxation and creep respectively via a finite series of exponentially decaying elements. One common method utilizes a Prony series of the form $\sum_{i=1}^{N} \alpha_i . e^{-t/\tau_i}$ and provides a simple approach for fitting data obtained experimentally [27, 28].

When the generalized Maxwell model is used to describe the behavior of the material, the stress-relaxation response is represented with a Prony series as follows:

$$E(t) = E_{\infty} + \sum_{i=1}^{n} E_i e^{-t/\tau_i} \qquad \text{(Eq. 5)}$$

where E_{∞} is long-term elastic modulus, E_i are the stress-relaxation elastic moduli associated with relaxation times τ_i related to each Prony component by the viscosities of the dashpots, $\tau_i \equiv \frac{\eta_i}{E_i}$.

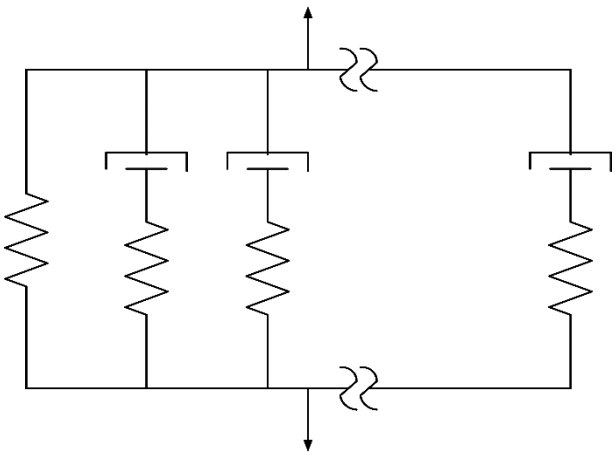

A. Generalized Maxwell Model

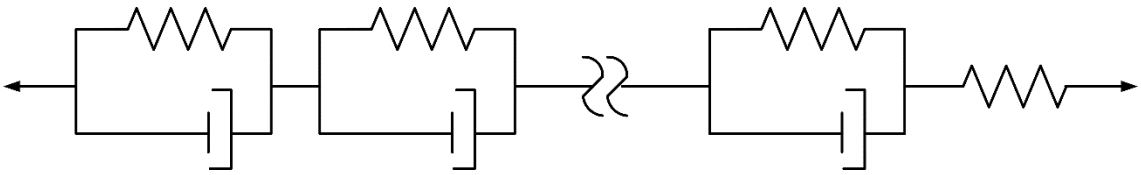

B. Generalized Voigt/Kelvin Model

Figure 5: Generalized A. Maxwell, B. Voigt/Kelvin Models

2.2. Fracture Mechanics

Barbed sutures can be regarded as suture wires with incisions introduced into their periphery to form barbs that, consequently, act as pre-existing cracks. The time-dependent propagation of cracks in polymeric materials has been investigated, whether theoretically or experimentally, by a number of researchers including Williams [29, 30], Vincent and Gotham [31], Kostrov and Nikitin [32], Knauss [33-35], Schapery [36-39], McCartney [40-42], Christensen et al. [43, 44], and Williams and Marshall [45-47].

Many of these theoretical developments are based on Linear Elastic Fracture Mechanics (LEFM) extended to viscoelastic behavior. In particular, Schapery [36, 37] demonstrated that the traditional fracture mechanics developed by Barenblatt for metals [48] can be applied to viscoelastic media by replacing the elastic modulus with a time-dependent viscoelastic modulus evaluated at a fictive time using linear viscoelasticity. Furthermore, he established a relatively simple analytical equation relating the applied stress intensity to the steady-state crack growth rate [49-51].

For a material with a preexisting crack subjected to loading, Schapery divides the medium into two regions; a highly non-linear region at the crack tip called the process zone and a linear viscoelastic region termed the far field region, appropriately distanced from the tip (Fig. 6). In this linear region, Schapery demonstrates that the stress distribution can be calculated using Barenblatt's relationship for elastic materials and that singularities cancel at the tip of the process zone if:

$$K_1 = \left(\frac{2}{\pi}\right)^{1/2} \int_0^{\alpha} \sigma_f(r) / r^{1/2} dr \qquad \text{(Eq. 6)}$$

where α is the length of the process zone and σ_f is the stress in the process zone as a function of r, the distance from the crack tip.

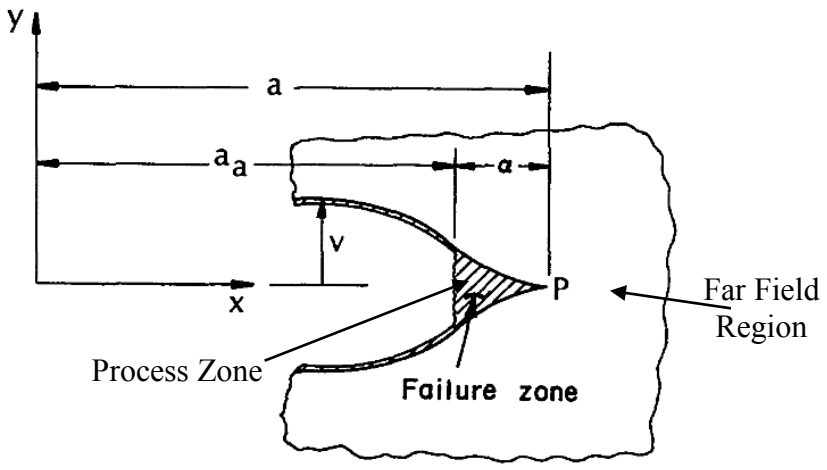

Figure 6: Schapery's Crack tip model [36]

In addition, the propagation of a crack at the boundary of the process zone can be approximated by the elastic solution when the elastic compliance is substituted with the viscoelastic creep compliance. Hence, Schapery determined an expression for the work required for the growth of the crack tip and, likewise, the process zone ultimately leading to failure by:

$$2\Gamma = \int_0^{\alpha} \frac{v(t,r)}{r} \sigma_f(r) dr \qquad \text{(Eq. 7)}$$

where Γ is the work per unit area of the fracture surface, $v(t,r)$ is the displacement at the boundary of the failure zone. In other words, the surface energy required for a crack to propagate is the product of the stress and displacement integrated over the boundary of the process zone.

Combining equations 6 and 7, and applying some manipulations, the following form is obtained for surface energy:

$$2\Gamma = C_v\left(\tilde{t}\right)K_1^2 \qquad \text{(Eq. 8)}$$

where $C_v\left(\tilde{t}\right)$ is the viscoelastic creep compliance as a function of the effective time $\tilde{t}$, which is the time required for viscoelastic deformation to take place in the process zone and is defined as:

$$\tilde{t} = d\,\frac{\alpha}{\dot{a}} \qquad \text{(Eq. 9)}$$

where $\dot{a}$ is the crack growth rate and d is a proportionality constant related to the exponent n in the simple power law representation of the creep compliance $C_v(\tilde{t}) = C_0 + C_1\tilde{t}^n$ where C_0 is the elastic component.

In fact, 2Γ is defined to be equal to G_{1c}, the critical strain energy release rate or simply, toughness. Hence,

$$G_{1c} = C_v\left(\tilde{t}\right)K_1^2 \qquad \text{(Eq. 10)}$$

And according to Griffith, crack propagation occurs when the elastic energy released per unit area of crack growth exceeds the required work of fracture per unit area of the created surfaces. For an elastic wide plate containing a through crack of length "$2a$", the nominal stress that causes fracture is:

$$\sigma_a \geq \sqrt{\frac{2\Gamma E'}{\pi a}} \qquad \text{(Eq. 11)}$$

where E' is the equivalent elastic modulus, $E' = E$ for plane stress and $E' = E/(1-\nu^2)$ for plane strain.

Also, from linear elastic fracture mechanics,

$$K_1 = \sigma\sqrt{\pi a} \qquad \text{(Eq. 12)}$$

Rearranging equations 11 and 12 yields the known relationship between G_I and K_I, $K_1^2 \geq G_{1c}E^{'}$. This equation is similar to the one obtained by Schapery for viscoelastic material except that $C_v\left(\tilde{t}\right)$ replaces the equivalent elastic modulus. Therefore, crack growth in viscoelastic material is distinguished from that in elastic medium by a time-dependent release of at least some portion of the elastic energy giving rise to a time-dependent propagation rather than an instantaneous one.

Furthermore, taking into consideration the Dugdale [52] assumption where a uniform stress exists in the process zone, Schapery derives a relationship between the applied stress intensity and the steady-state crack growth rate based on the aforementioned equations:

$$\dot{a} = \frac{\pi}{8}\left(\frac{C_1 d}{G_{1c} - K_1^2 C_0}\right)^{1/n} K_1^{n(1+1/n)} \qquad \text{(Eq. 13)}$$

where n is approximately equal to 1/3.

CHAPTER 3

METHODOLOGY

3.1. Experimentation

The viscoelastic constants required for material definition in finite element modeling were determined by performing a series of tensile and stress-relaxation experiments. Tests were performed using unbarbed 1 polypropylene sutures (PROLENE). According to the USP suture standard, the nominal diameter of the samples is between 0.4 - 0.499mm. A micrometer was used to measure the diameter of every specimen at the start of each experiment.

3.1.1. Tensile Test

The modulus of elasticity, poisson ratio and tensile breaking strength are of great interest when assessing the performance of sutures.

A universal testing machine (Lloyd Instruments, LS1) was used to carry out loading to failure tests on 12 suture specimens. A 1kN load cell was used and a strain rate of 25mm/min was applied for a gauge length of 10cm [53].

To avoid specimen slippage and grip-induced failures, customized mounting tabs were manufactured from 2.35mm thick medium-density fiberboard (MDF) using a laser cutting machine (Fig. 7) and pneumatic grips with rubber jaw faces (Lloyd Instruments) were installed (Fig. 8). According to ASTM Standard C1557 – 14, the gripping system should ensure axial alignment of the suture sample along the line of

action of the tensile testing machine such that neither spurious bending strains nor stress concentrations are induced [53]. The adapted mounting tabs along with the grips having uniform nonslip adherent surfaces make it possible to satisfy all the aforementioned conditions without damaging the specimen.

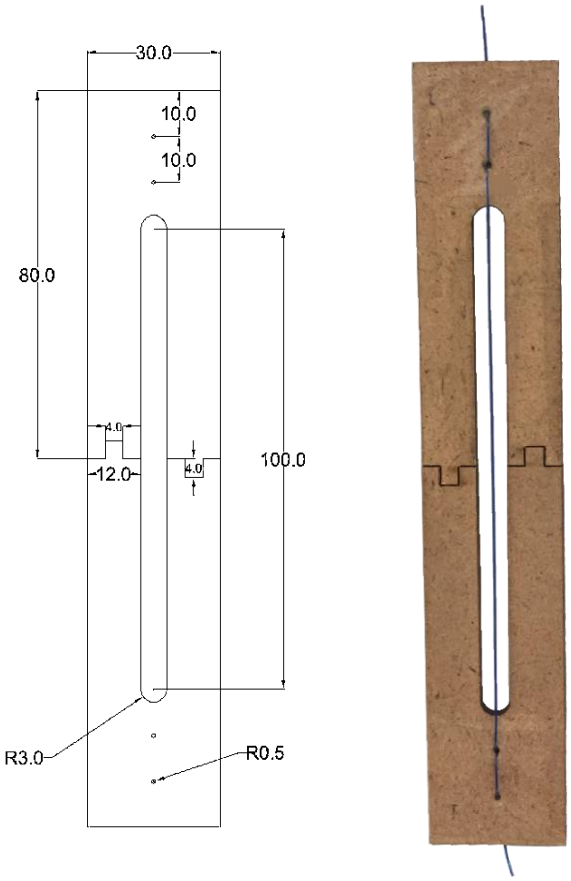

Figure 7: Manufactured customized mounting tabs

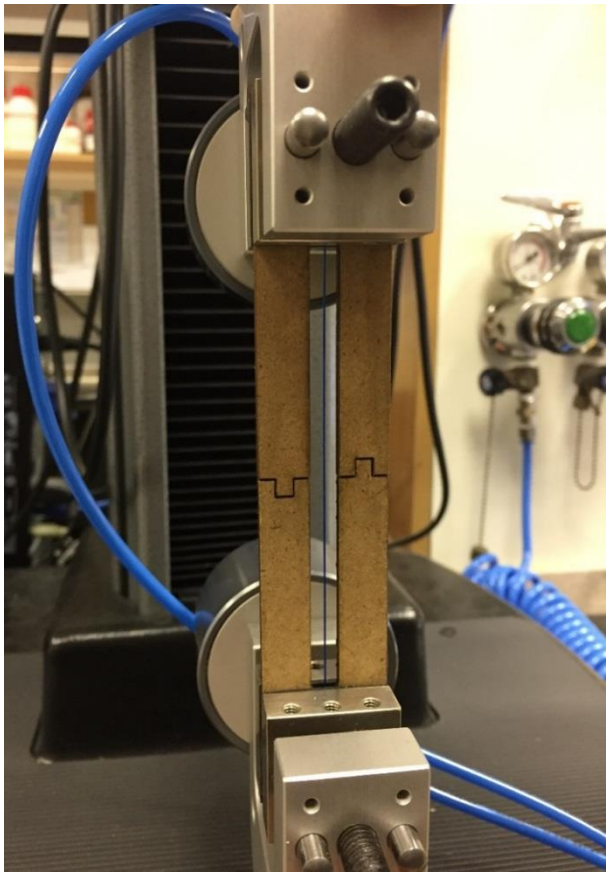

Figure 8:The experimental setup showing the suture sample anchored into the mounting tab and held with pneumatic grips

NEXYGENPlus materials testing software was used for test setup and for data collection and analysis. As aforementioned, a tension test was chosen with a preload of 5N at a speed of 25mm/min, and an extension rate of 25mm/min. The sample height was specified as the gauge length. The diameter of each suture sample obtained by averaging three measurements taken by a digital micrometer (Mitutoyo Series 293) from three different positions was inputted into the software to determine the sample area. In addition to the variation of stresses (forces) and strains (displacements) throughout the test, other essential results that include Young's Modulus, Tensile Strength, and Load (Stress) and Extension (Strain) at break were requested to be reported.

The engineering stresses and longitudinal strains were obtained directly from the recorded variations in tensile force and specimen length with time where the stress is the force divided by the initial cross-sectional area of the suture and the longitudinal strain is simply the change in the gauge length of the specimen divided by the initial gauge length.

$$\sigma = \frac{F}{A_0} \qquad \text{(Eq. 14)}$$

and

$$\varepsilon_x = \frac{\Delta \ell}{\ell_0} \qquad \text{(Eq. 15)}$$

As for the elastic modulus E, it was calculated from Hooke's law applied in the elastic region:

$$E = \frac{\sigma}{\varepsilon_x} \qquad \text{(Eq. 16)}$$

Attaining a value for the poisson ratio ν requires that the lateral strain be measured. Since the uniaxial testing machine is not equipped with gauges to keep a log of the shrinkage in suture diameter, the digital micrometer was used to measure the specimen diameter during tensile testing every 5seconds. The lateral strain is the ratio of the change in diameter to the initial value.

$$\varepsilon_y = \frac{\Delta d}{d_0} \qquad \text{(Eq. 17)}$$

and

$$\nu = -\frac{\varepsilon_y}{\varepsilon_x} \qquad \text{(Eq. 18)}$$

3.1.2. Relaxation Test

In order to determine the viscoelastic characteristics of polypropylene, a stress-relaxation test was performed. Using UTM machine (Fig. 8), a 0.1 mm/mm strain was attained at a rate of 25mm/min and was held constant for 60 minutes. The gradual decrease of the stress over the relaxation time period was recorded. The experiment was repeated for 10 different samples.

A curve fitting analysis of the obtained experimental data yields the prony series coefficients required as input for the definition of the viscoelastic material properties in the finite element model. This was performed with ABAQUS by inputting normalized shear relaxation data with respect to the initial stress as well as the respective time instants. The normalized shear stress relaxation modulus is expressed as a prony series by [54]

$$g(t) = 1 - \sum_{k=1}^{N} g_k (1 - e^{-t/\tau_k}) \qquad \text{(Eq. 19)}$$

where g_k is the normalized shear modulus $g_k = G_k / G_0$, G_0 is the instantaneous shear modulus determined from the instantaneous elastic modulus and poisson ratio $G_0 = E_0 / 2(1+\nu_0)$ and τ_k are the relaxation times. The sum of the dimensionless shear relaxation moduli g_k cannot exceed 1.

3.1.3. Fracture Toughness

Fracture toughness characterizes the ability of a material containing a crack to resist crack propagation and ultimately, full rupture. The propagation of a crack generally occurs due to the combined action of Mode I, Mode II, and Mode III loadings; that is, when the crack is subjected to both normal and shear displacements [55]. One of the most widely used mixed-mode fracture criteria is the power law criterion [56]. Each component of the fracture toughness is normalized by its critical pure-mode value and is expressed as a power law function.

For a combined Mode I and Mode II fracture envelope, the power law follows the empirical equation suggested by Richard [57]:

$$\left(\frac{G_I}{G_{Ic}}\right)^{\alpha} + \left(\frac{G_{II}}{G_{IIc}}\right)^{\beta} = 1 \qquad \text{(Eq. 20)}$$

This criterion allows for the modeling of a broad range of material responses by varying the values of α and β. For $\alpha = \beta = 1$, a linear relation is obtained and the mixed-mode linear criterion is realized. A concave curve is produced for $\alpha = \beta < 1$, while a convex one is generated for $\alpha = \beta > 1$. Responses generated for different combinations of α and β are shown in Fig. 9. For a specific material response, the optimal values for α and β are determined via a fitting analysis of the experimental data obtained under combined mode I and mode II loadings [58].

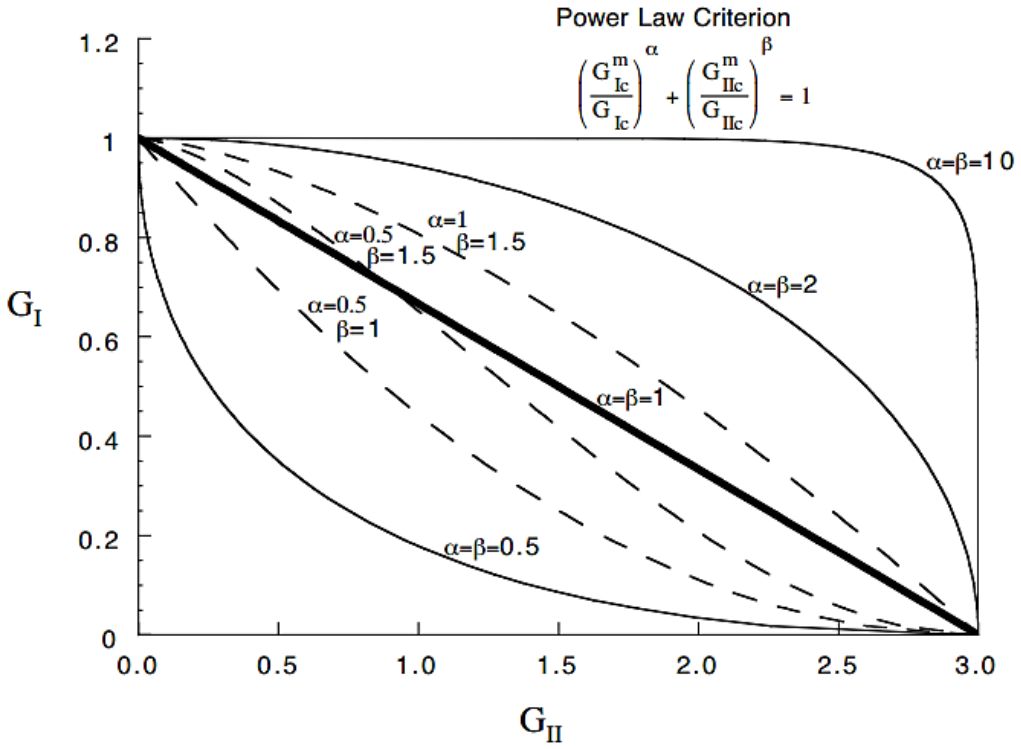

Figure 9: Response of power law criterion for different combinations of α and β [58]

The two-dimensional relation can be easily extended into a three-dimensional power law criterion consisting of six fitting parameters [56]:

$$\left(\frac{G_I}{G_{Ic}}\right)^{\alpha} + \left(\frac{G_{II}}{G_{IIc}}\right)^{\beta} + \left(\frac{G_{III}}{G_{IIIc}}\right)^{\chi} = 1 \qquad \text{(Eq. 21)}$$

Where G_{IC}, G_{IIC} and G_{IIIC} are the critical values of strain energy release rate; i.e. the fracture toughness, for the three orthogonal modes of loading, mode I (opening), mode II (sliding shear), and mode III (tearing shear) respectively. The powers, α, β and χ are curve fitting parameters.

Saito and Yoda [55] investigated the fracture toughness of polypropylene under combined Mode I and Mode II loadings. They obtained the Mode I – Mode II fracture toughness envelope and performed a fitting analysis for the resulting curve to determine

the best fit of the power law criterion. The values for the powers α and β were found to be 1 and 2 respectively. As such, the empirical equation for polypropylene is expressed as:

$$\left(\frac{G_I}{G_{Ic}}\right)^1+\left(\frac{G_{II}}{G_{IIc}}\right)^2=1 \qquad \text{(Eq. 22)}$$

Also, Saito and Yoda indicated that the ratio of Mode II fracture toughness to that of Mode I is equal to $(0.44)^2$. Hence, the mixed-mode power law criterion for polypropylene can be represented as:

$$\frac{G_I}{G_{Ic}}+\left(\frac{G_{II}}{0.1936G_{Ic}}\right)^2=1 \qquad \text{(Eq. 23)}$$

Experiments to obtain the mixed-mode fracture toughness of polypropylene were not performed due to the unavailability of the proper setup. The needed parameters are used as obtained from the literature [55] and are detailed in the Material Modeling section.

3.2. Finite Element Analysis

3.2.1. Viscoelastic Model

Linear viscoelasticity can be modeled in ABAQUS by a shear stress relaxation modulus expressed as a prony series by [54]

$$G(t)=G_0\left(1-\sum_{k=1}^{N}g_k(1-e^{-t/\tau_k})\right) \qquad \text{(Eq. 24)}$$

Where G_0, the instantaneous shear modulus is determined from the instantaneous elastic modulus and poisson ratio $G_0 = E_0/2(1+\nu_0)$ and τ_k are the relaxation times. The sum of the dimensionless shear relaxation moduli g_k cannot exceed 1.

The material bulk modulus can be expressed in a similar manner.

$$K(t) = K_0\left(1-\sum_{k=1}^{N} k_k(1-e^{-t/\tau_k})\right) \qquad \text{(Eq. 25)}$$

Where K_0, the instantaneous bulk modulus is also determined from the instantaneous elastic modulus and poisson ratio $K_0 = E_0/3(1-2\nu_0)$. The sum of the dimensionless bulk moduli k_k cannot exceed 1.

The input parameters required for the prony series were obtained from the number of stress-relaxation tests conducted on the polypropylene sutures.

3.2.2. Extended Finite Element Method

In this work, the crack propagation in a barbed suture under static loading conditions is of interest. For modeling discontinuities, such as cracks, in ABAQUS, an extended finite element method (XFEM) is implemented [54]. This method, as its name indicates, is an extension of the conventional finite element method and is also based on the concept of partition of unity. Contrary to traditional FEM that allows for crack propagation only along a preset path that coincides with the elements' boundaries, XFEM utilizes enrichment shape functions and allows for the presence of discontinuities within an element. As such, the mesh is not required to match the geometry of the crack. Hence,

the crack propagates along a solution-dependent path without the need to remesh the bulk material. Most importantly, XFEM allows for both material and geometrical nonlinearities; thus, it is applicable for the case of viscoelastic material.

For the nodes around the crack, the enriched displacement fields are expressed as:

$$u^h(x) = \sum_{I \in N} N_I(x) \left[u_I + H(x) a_I + \sum_{\alpha=1}^{4} F_\alpha(x) b_I^\alpha \right] \qquad \text{(Eq. 26)}$$

Where the term N_I represents the shape functions, u_I is the nodal displacement vectors for conventional shape functions, $H(x)$ is a Heaviside step function and a_I is nodal enriched degree of freedom vector where the term $H(x)a_I$ describes the displacement of the nodes pertaining to elements cut by the propagating crack, $\sum_{\alpha=1}^{4} F_a(x)$ is asymptotic crack tip functions and b_I^α is nodal enriched degree of freedom vector where the term $\sum_{\alpha=1}^{4} F_\alpha(x) b_I^\alpha$ describes the displacement of the nodes of the elements inclosing the crack tip. Hence, the behavior of three different types of elements are included in the XFEM method, the conventional elements, elements cut by the propagating crack, and elements at the crack tip (Fig. 10).

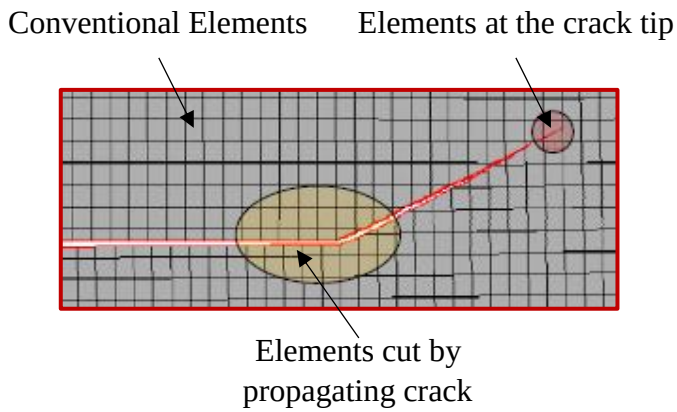

Figure 10: Three types of elements included in XFEM [59]

The location of a crack is determined in XFEM by the Level Set Method (LSM), which employs two functions, ϕ and ψ, where ϕ denotes the signed distance between a node and the face of the crack and ψ represents the signed distance between a node and an orthogonal plane passing through the crack tip (Fig. 11).

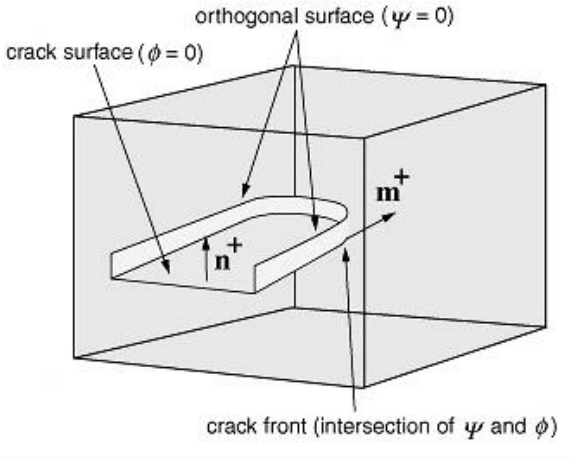

Figure 11: Level set method (LSM) [54]

3.2.3. Damage Initiation and Evolution Laws

Damage modeling in ABAQUS requires the definition of a damage initiation criterion and a damage evolution law. Once the initiation criterion is met, damage proceeds according to the specified evolution law.

In this analysis, the damage initiation criterion is defined by traction separation laws, specifically maximum principal stress (Maxps). The failure of the elements by this criterion is characterized by the progressive degradation of the material stiffness, which is itself driven by a damage process.

A traction separation law is defined by a nominal traction stress vector, t, which consists of three components in three-dimensional problems: t_n, t_s and t_t [54]. These components represent the normal and the two shear tractions, respectively. As for the corresponding separations, they are denoted by δ_n, δ_s, and δ_t. The original thickness of the element is denoted by T_0, and likewise, the nominal strains can be expressed as

$$\varepsilon_n = \frac{\delta_n}{T_0},\ \varepsilon_s = \frac{\delta_s}{T_0},\ \varepsilon_t = \frac{\delta_t}{T_0} \qquad \text{(Eq. 27)}$$

Hence, the elastic behavior can then be stated as

$$t = \begin{Bmatrix} t_n \\ t_s \\ t_t \end{Bmatrix} = \begin{bmatrix} K_{nn} & K_{ns} & K_{nt} \\ K_{ns} & K_{ss} & K_{st} \\ K_{nt} & K_{st} & K_{tt} \end{bmatrix} \begin{Bmatrix} \varepsilon_n \\ \varepsilon_s \\ \varepsilon_t \end{Bmatrix} = K\varepsilon \qquad \text{(Eq. 28)}$$

The elasticity matrix describes the fully coupled behavior between all components of the traction vector and the separation vector. For an uncoupled behavior between the normal and shear components, the off-diagonal terms in the elasticity matrix can be set to zero.

Rate-dependent behavior of elements can be modeled with traction-separation elasticity, and as such traction separation laws can be applied in combination with linear viscoelasticity. In this case, the evolution equations for the normal and two shear nominal tractions are expressed as:

$$t_n(t) = t_n^0(t) + \int_0^t \dot{K}_R(s)\, t_n^0(t-s)ds \qquad \text{(Eq. 29)}$$

$$t_s(t) = t_s^0(t) + \int_0^t \dot{g}_R(s)\, t_s^0(t-s)ds \qquad \text{(Eq. 30)}$$

$$t_t(t) = t_t^0(t) + \int_0^t \dot{g}_R(s)\, t_t^0(t-s)ds \qquad \text{(Eq. 31)}$$

Where $t_n^0(t)$, $t_s^0(t)$, and $t_t^0(t)$ are the instantaneous nominal tractions at time t in the normal and the two local shear directions, respectively. The functions $g_R(t)$ and $K_R(t)$ represent the dimensionless shear and normal relaxation moduli, respectively.

For the maximum principal stress (Maxps) criterion in specific, damage initiation is represented as:

$$f = \left\{ \frac{\langle \sigma_{\max} \rangle}{\sigma_{\max}^0} \right\} \qquad \text{(Eq. 32)}$$

Where $\sigma_{\max}^0$ represents the maximum allowable principal stress. The symbol $\langle\ \rangle$ represents the Macaulay bracket, signifying that purely compressive stresses do not initiate damage. When the value of f reaches 1 within a prescribed tolerance, $1.0 \le f \le 1.0 + f_{tol}$, a new crack is initialized or an existing crack propagates.

To describe the evolution of damage based on the principles of LEFM, a critical strain energy release rate criterion is defined. In the general case involving Modes I, II,

and III, crack propagation occurs when the equivalent strain energy release rate at the crack tip exceeds the specified critical equivalent strain energy release rate. In other words, the fracture criterion is expressed as [54]:

$$f = \frac{G_{equiv}}{G_{equivC}} \geq 1 \qquad \text{(Eq. 33)}$$

Where G_{equiv} is the equivalent strain energy release rate calculated at a node, and G_{equivC} is the critical equivalent strain energy release rate calculated based on the user-specified mode-mix criterion and the bond strength of the interface.

In this analysis, power law model is specified as the mode-mix criterion and is described for Modes I, II, and II by the following formula:

$$\frac{G_{equiv}}{G_{equivC}} = \left(\frac{G_I}{G_{IC}}\right)^{a_m} + \left(\frac{G_{II}}{G_{IIC}}\right)^{a_n} + \left(\frac{G_{III}}{G_{IIIC}}\right)^{a_o} \qquad \text{(Eq. 34)}$$

Where G_{IC}, G_{IIC} and G_{IIIC} are the critical values of strain energy release rate; i.e. the fracture toughness, for the three orthogonal modes of loading, mode I (opening), mode II (sliding shear), and mode III (tearing shear) respectively. The powers, a_m, a_n and a_o are curve fitting parameters.

CHAPTER 4

FINITE ELEMENT MODELLING

4.1. Geometry

The finite element analysis of the barbed suture was implemented on ABAQUS 6.14. The geometric model consists of a three-dimensional deformable cylinder with an elliptical cross-sectional area to represent the suture, whereas the barb (crack) is introduced as a cell partition. Simulations were performed while varying three main factors: aspect ratio of the ellipse (ρ) on one hand, and cut angle and cut depth of the barb on another.

Initial studies rely on geometric dimensions of commercially available barbed sutures in order to gain insight regarding their performance. Existing sutures have a circular cross-sectional area; that is, $\rho = 1$, and on average, a cut angle of 154° and a cut depth of 0.19mm [60-62]. Thus, as a starting point, a circular suture of diameter 0.6mm (USP 2), length 1mm, cut angle 154°, and cut depth of 0.19mm is considered.

4.1.1. Cross-Sectional Area of Flexor Tendons

The main motivation behind varying the aspect ratio of the suture arises from the elliptical nature of the flexor tendons cross-section (Fig.12). It is anticipated that better conformity between the suture and the tendon is achieved when both possess similar aspect ratios. Widths and heights of flexor digitorum superficialis and profundus tendons (FDST and FDPT respectively) corresponding to index, middle, ring, and little fingers

were obtained from the literature [63, 64], in order to evaluate their aspect ratios and gain insight on possible design values for ρ . The dimensions are summarized in table 1.

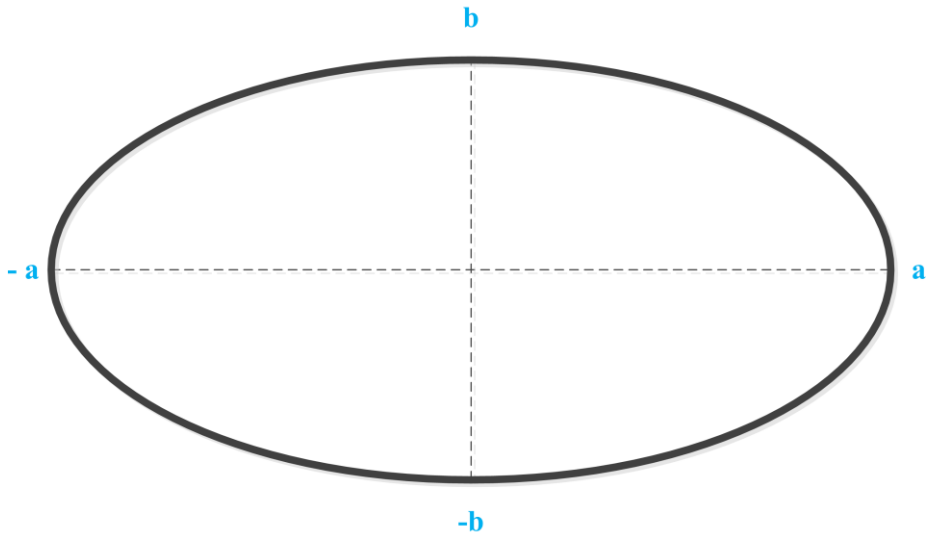

Figure 12: Schematic of an ellipse cross-section showing major and minor axes

		Index	Middle	Ring	Little
FDST	Major axis $\left(a=\frac{Width}{2}\right)$ (mm) [63]	2.5	3.25	2.75	1.5
	Cross-sectional Area (CSA) (mm^2) [64]	8.36	11.54	10.46	4.04
	Minor axis $\left(b=\frac{Height}{2}=\frac{CSA}{\pi a}\right)$ (mm)	1.0644	1.13	1.21	0.858
	Aspect Ratio $\left(\rho=\frac{a}{b}\right)$	2.35	2.88	2.27	1.75
FDPT	Major axis $\left(a=\frac{Width}{2}\right)$ (mm) [63]	2.5	3	2.5	2.25
	Cross-sectional Area (CSA) (mm^2) [64]	11.4	14.44	13.42	8.84
	Minor axis $\left(b=\frac{Height}{2}=\frac{CSA}{\pi a}\right)$ (mm)	1.452	1.532	1.708	1.25
	Aspect Ratio $\left(\rho=\frac{a}{b}\right)$	1.722	1.96	1.46	1.8

Table 1: Dimensions of FDST and FDPT

The dimensions of the smallest tendon should be taken as the reference design such that the developed suture is suitable for use on all flexor tendons. As table 1 shows, the FDST of the little finger has the smallest major and minor axes; a=1.5mm, b=0.858mm. On average, the aspect ratio ρ is 2 and varies between a maximum of 2.88 for the FDST of the middle finger and a minimum of 1.46 for the FDPT of the ring finger.

Based on these findings, the values of ρ were varied between 1/3 and 3. The effect of the aspect ratio on the strength of the suture was investigated for constant cut angle and cut depth. Also, three different cut depths and cut angles: 0.07mm, 0.12 mm, and 0.19mm as depths and 150°, 154°, and 160° as angles were studied for a constant ρ. Furthermore, the radius of the suture (or the equivalent ellipse axes) was increased from 0.3mm to a larger diameter that is suitable with both the dimensions of the smallest tendon (FDST of little finger) and the optimum aspect ratio. It is desired that the optimized suture accommodates about 30% of the tendon's cross-sectional area. The diagram in figure 13 clarifies the scheme that was followed.

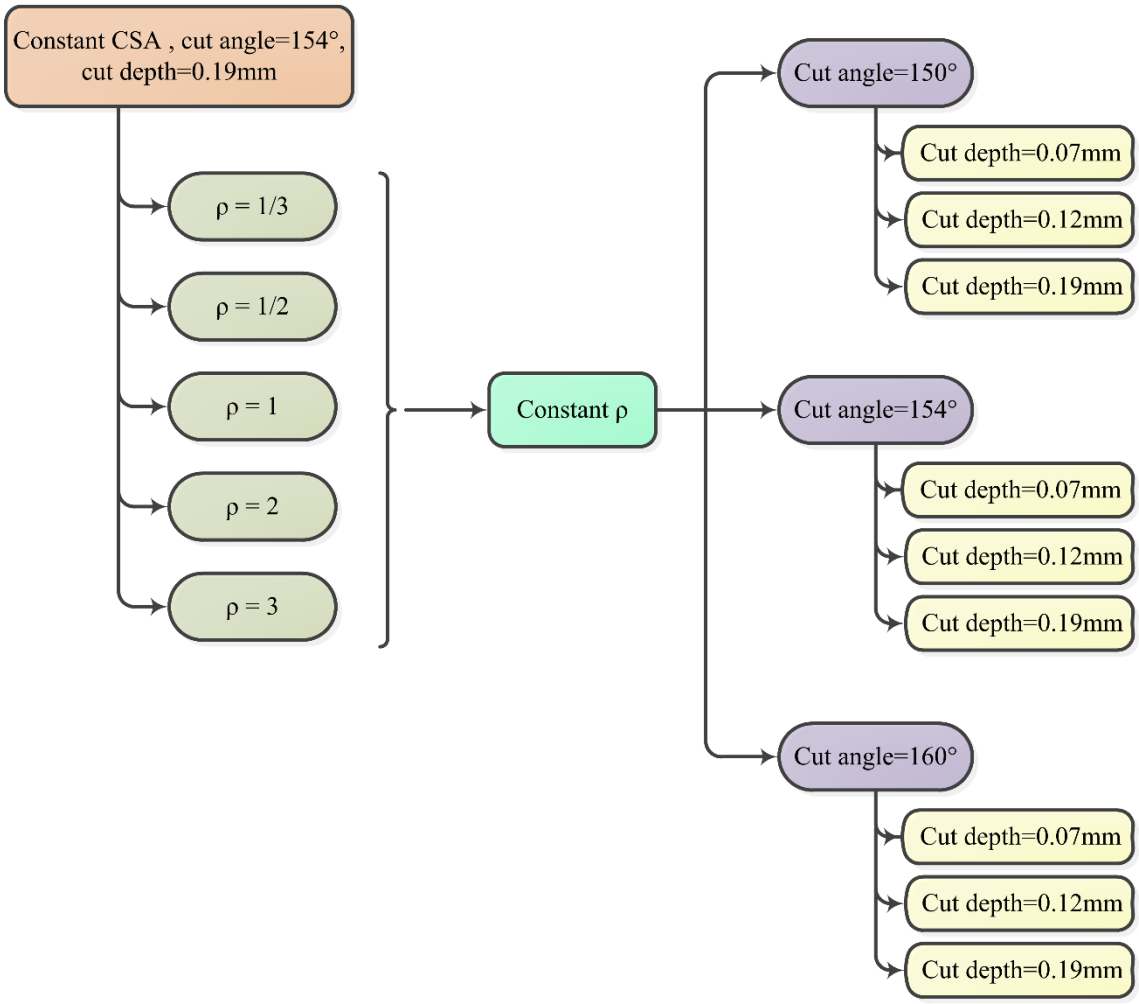

Figure 13: Flowchart clarifying the plan followed throughout the analysis

The values for diameter, cut angle, and cut depth were set for a circular cross-sectional area (CSA). When considering elliptical profiles, the major and minor axes were determined such that the area of the ellipse is equal to that of the circle. Furthermore, while the cut angles remain the same, the cut depths should be adapted for the ellipses in order to retain the same amount of intact area after inducing a cut in the sutures. The performed calculations are detailed below.

Finding major and minor axes:

$$(CSA)_{ellipse} = (CSA)_{circle} \quad \text{(Eq. 35)}$$

$$\pi ab = \pi r^2 \quad \text{(Eq. 36)}$$

And for an ellipse,

$$\rho = \frac{a}{b} \quad \text{(Eq. 37)}$$

Therefore,

$$a = r\sqrt{\rho} \quad \text{(Eq. 38)}$$

and

$$b = \frac{r}{\sqrt{\rho}} \quad \text{(Eq. 39)}$$

Finding equivalent cut depth:

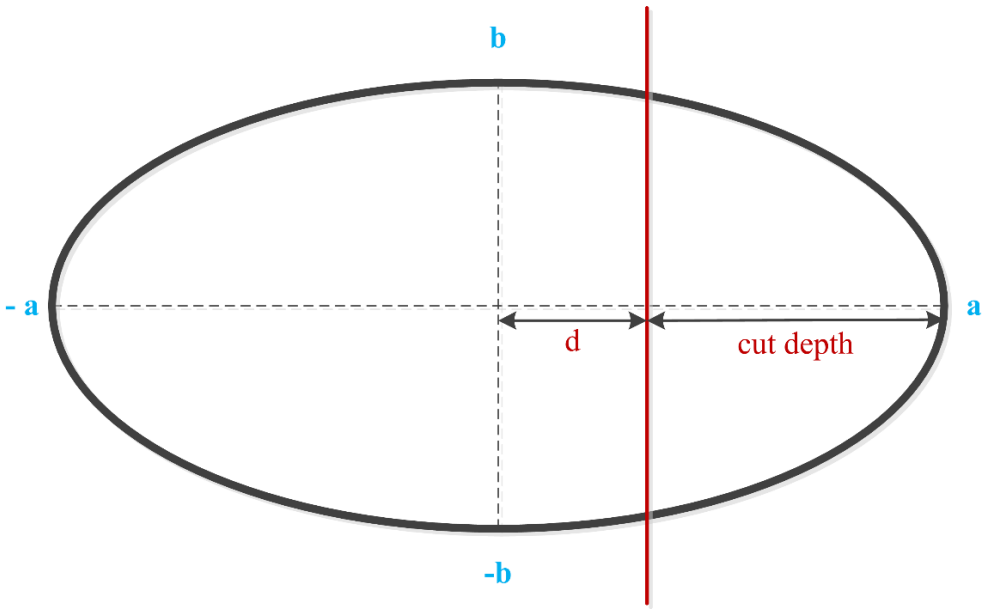

Figure 14: Diagram of an ellipse with a cut on its major axis

The remaining area of the ellipse in figure 14 can be found by using the following relation:

$$(RA)_{ellipse} = a*b*\left(\frac{\pi}{2}+\sin^{-1}\left(\frac{d}{a}\right)\right)+\frac{b*d*\sqrt{a^2-d^2}}{a} \qquad \text{(Eq. 40)}$$

where a and b are the major and minor axes respectively, and d is the distance from the center to the cut *(d= a – cut depth)* as shown in figure 14. Note that $\sin^{-1}\left(\frac{d}{a}\right)$ should be in radians.

Since the remining area of the ellipse should be equal to that of the circle, Eq.40 was used with $a = b = r$ (radius of the circle) along with the desired cut distance d in order to determine the remaining area of the circle. Once the latter was known, it was set as the remaining area of the ellipse and the equation was solved for the equivalent "d". The corresponding cut depth is simply found by subtracting the major axis from the cut distance; that is, *cut depth = a – d*.

The dimensions of the studied geometries to determine the most suitable aspect ratio are summarized in table 2.

	Ellipse Equivalence				
Aspect Ratio ρ = a/b	1/3	1/2	1	2	3
Major axis a (mm)	0.1732	0.2121	0.3	0.4243	0.5196
Minor axis b (mm)	0.5196	0.4243	0.3	0.2121	0.1732
Cross-sectional Area (CSA) (mm^2)	0.2827	0.2827	0.2827	0.2827	0.2827
Remaining Area (RA) (mm^2)	0.2059	0.2059	0.2059	0.2059	0.2059
Cut distance d (mm)	0.0635	0.0778	0.11	0.1556	0.1905
Cut depth (mm)	0.1097	0.1344	0.19	0.2687	0.3291

Table 2: Ellipse equivalent dimensions and cut depth

For simplification purposes, a single barb is included in the model. The different geometries used in this analysis are depicted in figure 15.

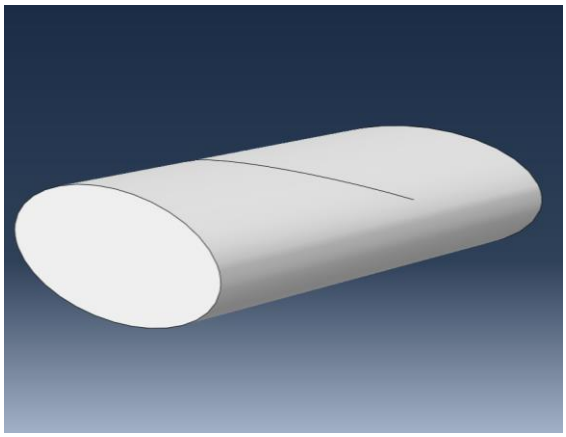

Aspect Ratio 1/3

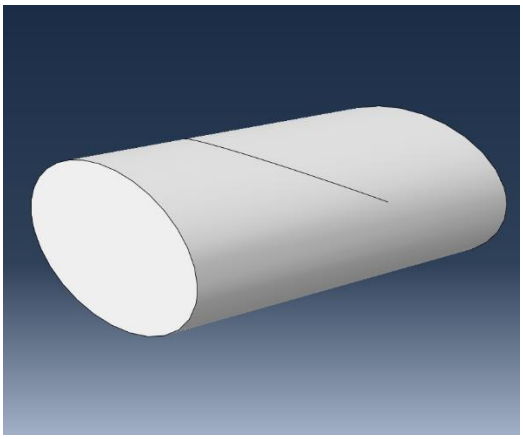

Aspect Ratio 1/2

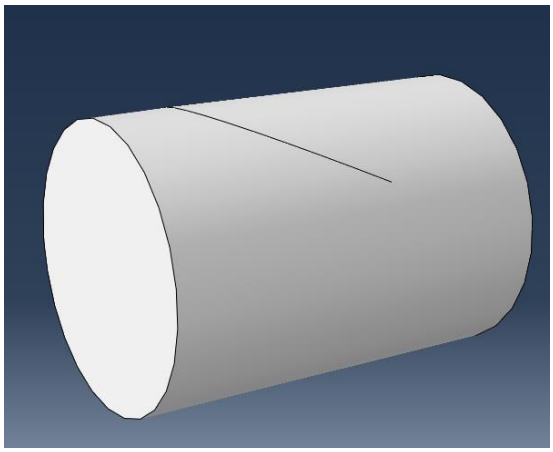

Aspect Ratio 1

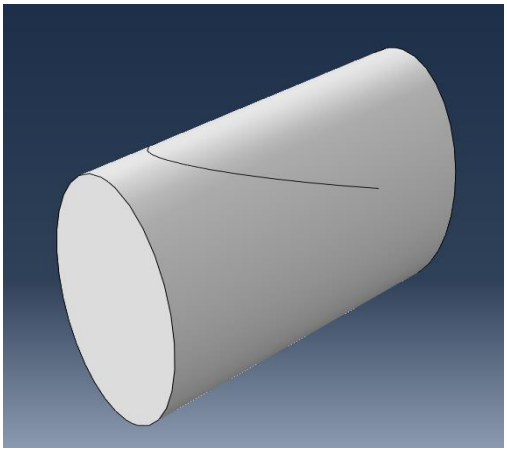

Aspect Ratio 2

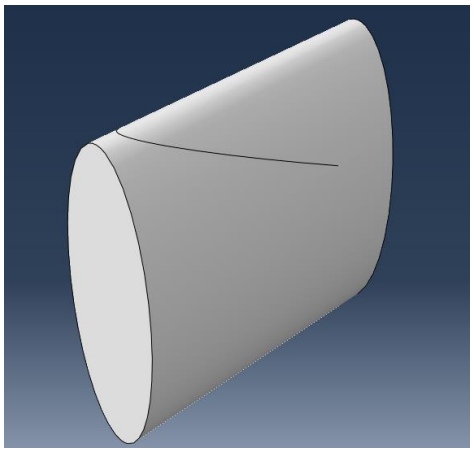

Aspect Ratio 3

Figure 15: Different geometries used in modelling

4.2. Material Modeling

The material properties of polypropylene were obtained as described in the experiment section above.

As aforementioned, tensile tests to failure were performed on 12 different suture specimens to determine polypropylene's short-term linear elastic behavior, which requires the definition of an instantaneous Young's Modulus and a Poisson's ratio. The averaged results for these two properties, in addition to the Tensile Strength are included in table 3. Their respective standard deviations are reported as well. Figure 16 shows the obtained stress-strain curve.

	Mean	Standard Deviation
Young's Modulus (MPa)	1668.67	573.37
Poisson's ratio	0.36878	0.06347
Tensile Strength (MPa)	353.15	48.81

Table 3: Elastic properties of polypropylene

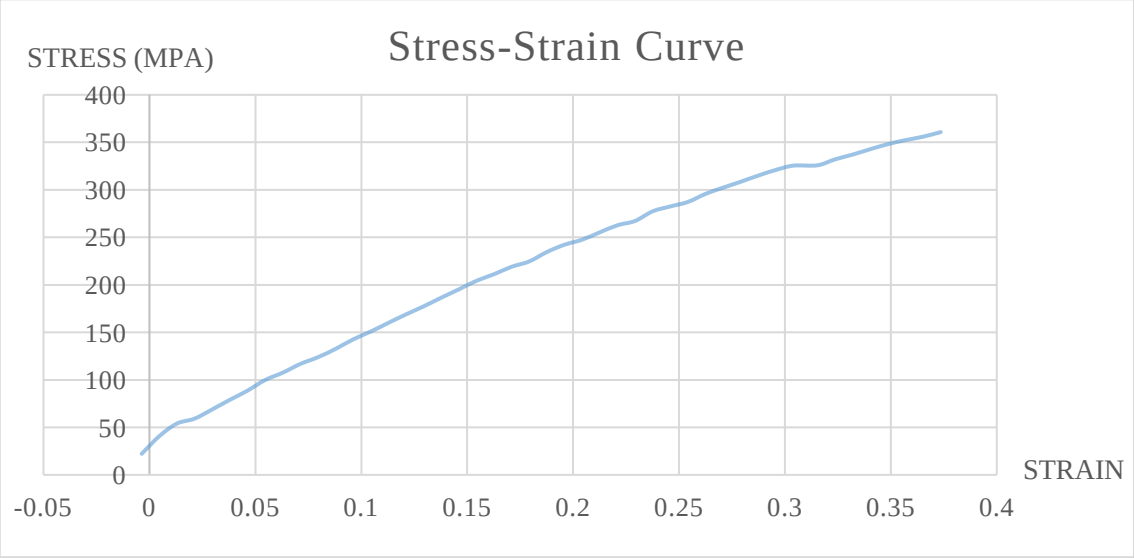

Figure 16: Stress-Strain curve for polypropylene obtained experimentally

The time-dependent behavior, on the other hand, was specified as previously described, via inputting into ABAQUS normalized shear relaxation data with respect to the initial stress along with the respective time instants as obtained from the relaxation tests. ABAQUS then performs a curve fitting analysis to determine the prony series coefficients. The computed values for the normalized shear g_i and bulk k_i moduli, in addition to the corresponding relaxation times τ_i are listed in table 4. A plot of the normalized stress relaxation behavior and its curve fit is shown in figure 17.

It is noteworthy to point out that the relaxation times gotten from experimentation were scaled by 100 when inputted into ABAQUS such that the total time becomes 36s instead of 3600s (60 minutes). This was done in order to avoid lengthy simulations and to be able to capture polypropylene's relaxation behavior within the model.

i	**g_i**	**k_i**	**τ_i**
1	0.31542	0	0.63594
2	0.32027	0	10.243

Table 4: Prony series coefficients for polypropylene obtained from ABAQUS

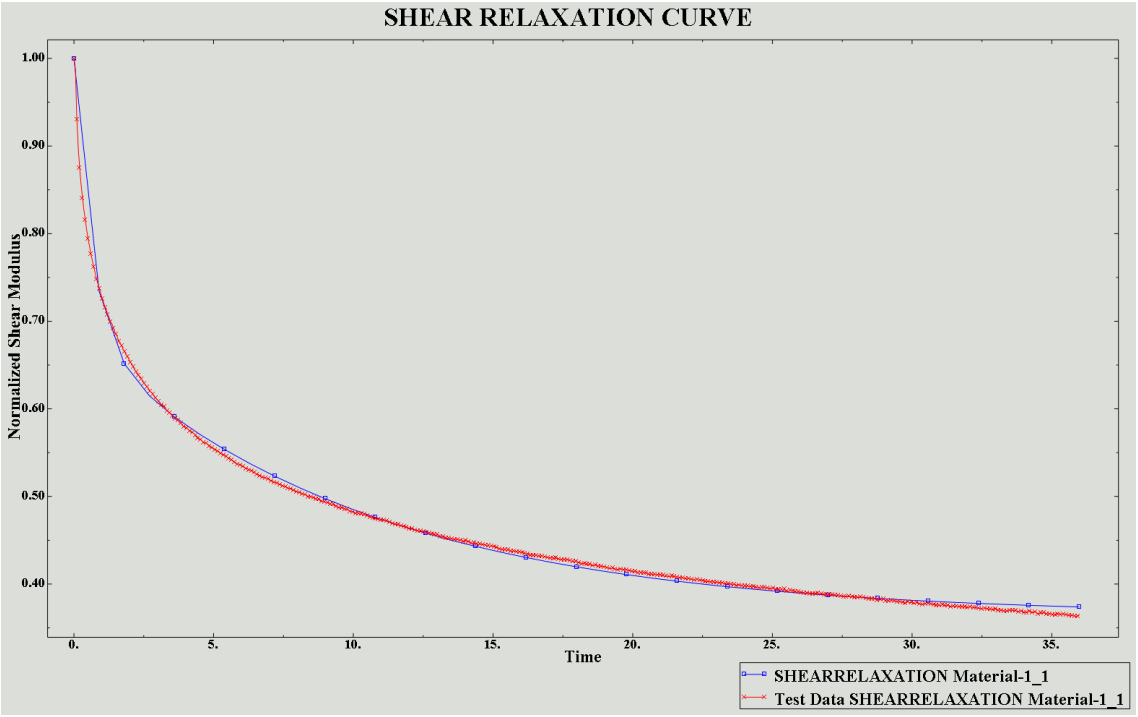

Figure 17: Shear Relaxation curve from experimental data (red) and ABAQUS curve fitting (blue)

As for damage initiation, the maximum principal stress was chosen. Since this criterion defines the nucleation of a defect within the body, and since the geometric model at hand has a crack already defined, the value for Maxps is not of high significance for this crack propagation analysis. The calculated true ultimate strength was used as the limiting maximum principal stress. The conversion of the engineering tensile strength (Table 3) obtained from tensile experiments to its true equivalent was done using the following relation:

$$\sigma_{true} = \sigma_{eng}\left(1+\varepsilon_{eng}\right) \qquad \text{(Eq. 41)}$$

Applying Eq. 41 to polypropylene:

$$\sigma_{true} = 353.147\left(1+0.39145\right) = 491.39MPa$$

As such, the value of Maxps was set at 491.39 MPa specified at the crack tip. For a mesh that is not sufficiently refined in the vicinity of the crack tip, the default centroidal approximation of the Maxps may not be accurate. It is recommended that the stresses be extrapolated to the crack tip [54]. As for tolerance, the default value of 0.05 was kept.

For a pre-existing crack, damage evolution is much more important for the analysis. Based on the principles of LEFM, a power law mixed mode energy-based criterion was selected with the power set as 1. The critical Mode I, Mode II, and Mode III energy release rates (G_{Ic}, G_{IIc}, and G_{IIIc} respectively) should be specified. These values were obtained as critical stress intensity factors K_{Ic} and K_{IIc} form the literature [55] and converted to values for G_{Ic} and G_{IIc} assuming plane strain conditions using the equations 42 and 43:

$$G_{Ic} = \frac{K_{Ic}^2\left(1-\nu^2\right)}{E} \qquad \text{(Eq. 42)}$$

$$G_{IIc} = \frac{K_{IIc}^2\left(1-\nu^2\right)}{E} \qquad \text{(Eq. 43)}$$

Where E is the Young's Modulus and ν is the Poisson's ratio.

For $K_{Ic} = 5.5\ MPa\sqrt{m}$, and $K_{IIc} = 0.44\ K_{Ic} = 2.42\ MPa\sqrt{m}$:

$$G_{Ic} = \frac{K_{Ic}^2\left(1-\nu^2\right)}{E} = \frac{\left(5.5\right)^2\left(1-0.36878^2\right)}{1668.67} = 15.663\,MPa.mm$$

and

$$G_{IIc} = \frac{K_{IIc}^2\left(1-\nu^2\right)}{E} = \frac{\left(2.42\right)^2\left(1-0.36878^2\right)}{1668.67} = 3.0323\,MPa.mm$$

Or alternatively,

$$G_{IIc} = (0.44)^2 G_{Ic} = 3.0323 \ MPa.mm$$

For Mode III, it was assumed that the critical energy release rate G_{IIIc} was equal to that of mode II due to the lack of fracture toughness data for this out-of-plane shear. As such, G_{Ic}, G_{IIc}, and G_{IIIc} were set to be equal to 15.663 *MPa.mm*, 3.0323 *MPa.mm*, and 3.0323 *MPa.mm* respectively.

For damage stabilization, viscous regularization was used to specify viscosity coefficients. When the model exhibits material softening and stiffness degradation, severe convergence problems arise. A viscous regularization scheme helps improve convergence by stabilizing the model during damage [54]. The value for the viscosity coefficient should be chosen such that stabilization does not significantly influence the final results. To make sure that this is the case, the viscous dissipation output (ALLVD) should be small compared to the strain energy (ALLSE). Throughout this analysis, viscous regularization was chosen to be 1E-005. ALLVD and ALLSE for a circular suture having a cut angle 154° and cut depth 0.19mm are shown in figure 18. ALLVD is nearly zero and is very small compared to ALLSE. Similarly, the selected value was checked for all other models to ensure that it did not affect the solution.

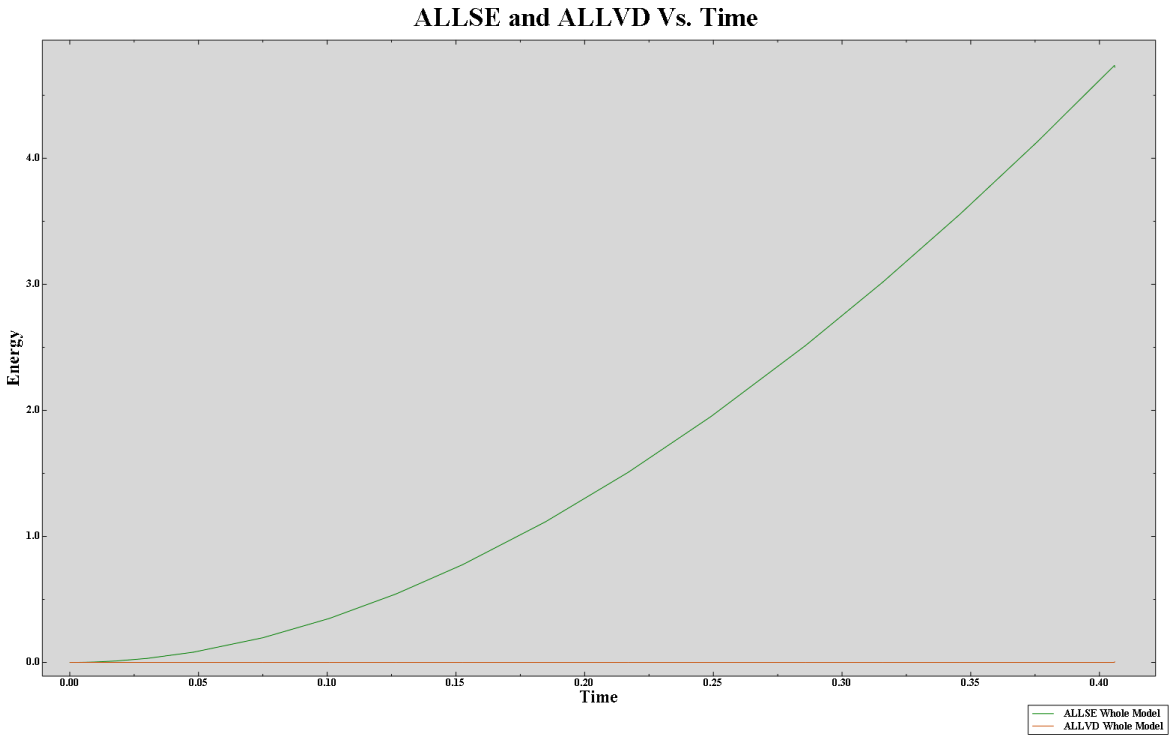

Figure 18: ALLSE and ALLVD for the whole model with respect to time

4.3. Configuring the Step Module

The time-dependent material properties defined require that a Visco Step be created in addition to the Initial step found by default and a Static General Step. The Static step was applied to initialize the elastic properties of the linear viscoelastic polypropylene and was assigned a very small time period of 0.001s and an initial increment size of 0.001s, minimum increment size of 1E-006s, maximum increment size of 0.001s, and maximum number of increments 100.

The viscoelastic properties are taken into account in the Visco procedure that follows. The Visco step was given a time period of 1.2s with an initial increment size of 0.01s, minimum increment size of 1E-030s, maximum increment size of 0.01s, and maximum number of increments 100000. Non-linear geometry (NLgeom) was toggled on for both steps to account for geometric nonlinearities.

Automatic time incrementation was chosen for both steps. ABAQUS selects the required increment sizes based on computational efficiency without any user intervention [54]. It is recommended to use automatic incrementation instead of fixed. For the latter case, the user should make sure that the specified time increment is small enough such that a stable solution is obtained. ABAQUS will not check if the solution is unstable. As such, valid results are not always attained.

For a model that contains a single material type, the time increment is directly proportional to the smallest element in the mesh. ABAQUS estimates the size of the stable time increment (Δt) by computing the time it takes a dilatational wave to transit across any of the mesh elements [54]:

$$\Delta t \approx \frac{L_{\min}}{c_d} \qquad \text{(Eq. 44)}$$

where $L_{\min}$ is the smallest element dimension in the mesh and c_d is the dilatational wave speed expressed in terms of λ_0 and μ_0 as:

$$c_d = \sqrt{\frac{\hat{\lambda} + 2\hat{\mu}}{\rho}} \qquad \text{(Eq. 45)}$$

such that for an isotropic elastic material, λ_0 and μ_0 are related to the Young's modulus E and Poisson's ratio ν by:

$$\hat{\lambda} = \lambda_0 = \frac{E\nu}{(1+\nu)(1-2\nu)} \qquad \text{(Eq. 46)}$$

and

$$\hat{\mu} = \mu_0 = \frac{E}{2(1+\nu)} \qquad \text{(Eq. 47)}$$

The stable time increment calculated from these relations is only an approximation that is not even conservative. For this reason, ABAQUS further reduces this Δt by a factor between $1/\sqrt{2}$ and 1 for two-dimensional models and between $1/\sqrt{3}$ and 1 for three-dimensional ones.

However, in cases where local instabilities, such as cracks, may arise, a quasi-static solution may not be attained, even when automatic incrementation is implemented. In order to overcome such difficulties, ABAQUS offers several methods for automatic stabilization whereby a damping is applied throughout the model. The introduced viscous forces due to damping are sufficiently large such that they stabilize the solution but at the same time, do not affect the solution significantly [54].

In this analysis, the method "Use damping factors from previous general step" was used for both steps. Damping factors at the end of the preceding step are used as the initial factors for the current step, overriding any specified damping for this current step. In case the current step is the first step in the model or the previous step was not stabilized, ABAQUS implements adaptive stabilization to decide on suitable damping factors.

With the adaptive stabilization scheme, the damping factor is determined based on the convergence history as well as the ratio of the energy dissipated due to viscous damping (ALLSD) to the total strain energy (ALLIE) [54]. ABAQUS may increase or decrease the damping factor based on the convergence behavior of the model. A maximum ratio of stabilization to strain energy is required for this method. For this model, the default value of 0.05 was kept, knowing that such value is suitable for most applications.

When automatic incrementation is selected for a Visco step, a "Creep /swelling / viscoelastic strain error tolerance" should be specified in order to limit the maximum permissible rate of change of the inelastic strain over an increment [54]. To ensure accuracy, the value for this tolerance is recommended to be, for creep problems, on the order of σ_{err}/E, where σ_{err} is a tolerable level of error in the stresses and *E* is the elastic modulus, or for problems involving viscoelasticity, is given a value on the order of the elastic strains. In this model, the "Creep /swelling / viscoelastic strain error tolerance" was set as 0.001.

Other adjustments to the setup may be applied for better convergence. The "discontinuous analysis" in the time incrementation tab of the general solution controls was selected. This allows for more iterations before checking the solution convergence and as such, avoid premature reductions of the time increments. Furthermore, the I_A parameter was increased from its default value of 5 to 30, such that more attempts (30 attempts instead of 5) are allowed before the simulation is aborted.

4.4. Crack Modeling

For the definition of the crack in ABAQUS, the suture geometry was selected as the domain while the barb created as a cell partition was specified as the crack (Fig. 19). An XFEM crack growth interaction was created and crack propagation was allowed in the initial step.

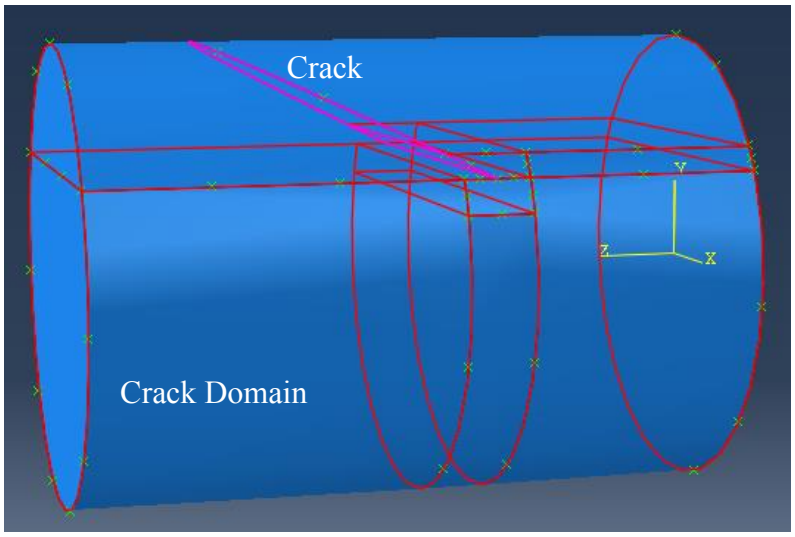

Figure 19: Defining the crack using XFEM

As aforementioned, XFEM based on VCCT was implemented as the fracture criterion to model crack propagation. A contact interaction property was created with energy-based mixed mode power law. Maximum tangential shear stress was chosen to be the direction of crack growth. A tolerance of 0.05 and viscosity of 1E-005 were specified. Tolerance for unstable crack propagation was toggled on and kept at its default value of 0.2.

Mode I, Mode II, and Mode III critical energy release rates were given the same values as those previously specified for the damage evolution criterion. As for the powers a_m, a_n and a_o, they were found in the literature to be 1, 2, and 1 respectively [55]. Table 5 summarizes the parameters required for the definition of the indicated fracture criterion.

Mode I	**Mode II**	**Mode III**	a_m	a_n	a_o
15.663	3.0323	3.0323	1	2	1

Table 5: Input for mixed-mode power law

In order to visualize a crack when using XFEM analysis, PHILSM and PSILSM should be requested as output. PSILSM is required to view the initial crack front, while PHILSM is necessary to observe the location of the crack. Also, the output STATUSXFEM should be chosen in order to perceive the status of the enriched elements. A value of 0 for this output means that the element is undamaged, a value of 1 means that the element has been completely cut by the crack, and a value in between 1 and 0 signifies that the element is damaged but some traction forces remain.

4.5. Boundary Conditions and Loads

The performance of the barbed suture was investigated under two loading conditions. The first case studies the strength of the suture and simulates a tensile test whereby one end is held fixed while the other is subjected to a finite displacement. The second case investigates the strength of a single barb. The boundary conditions are similar to those of the first load case, but in this analysis, the surface of the barb is constrained in the direction of application of the displacement.

4.5.1. Loading Case 1

For the geometry presented in figure 20, the right extremity was fixed by an ENCASTRE boundary condition applied in the initial step and propagated to the following Static and Visco steps. As for the left edge, a displacement/rotation boundary condition was specified at the surface. The displacement in z-direction, U3 was set to 0 initially. However, it was modified in the first Static step to a ramped displacement of magnitude 0.5mm and was propagated to the subsequent Visco step.

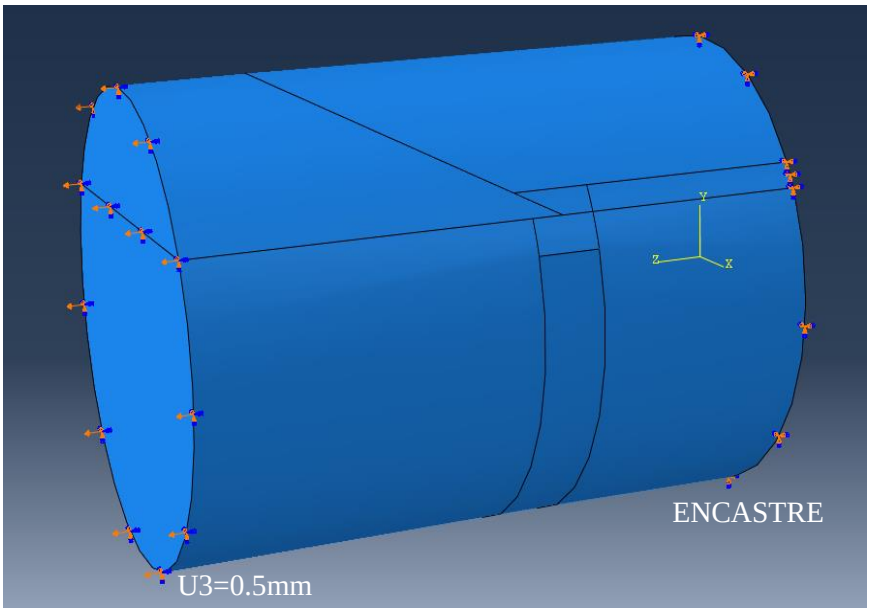

Figure 20: Boundary conditions for load case 1

Average stresses and strains in the body of the suture below the crack tip were of interest at the onset of failure. For this reason, an element set, Elem1, was created and associated with a Field Output Request to report strains and stresses in the z-direction, NE33 and S33 respectively. Figure 21 shows the location of Elem1 in a circular suture.

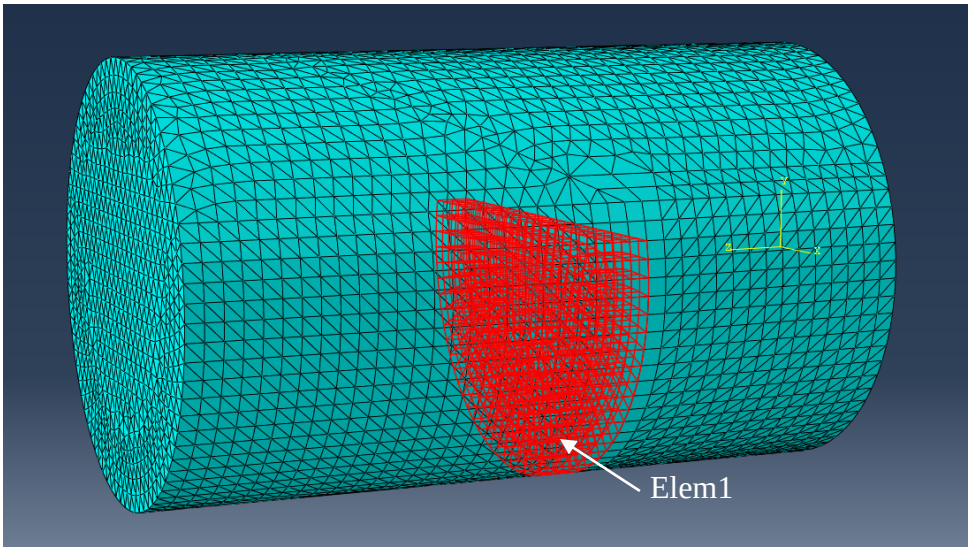

Figure 21: The position of Elem1 set highlighted in red

4.5.2. Loading Case 2

For the second test case, the left extremity was fixed by an ENCASTRE boundary condition applied in the initial step and propagated to the following Static and Visco steps. As for the right edge, a displacement/rotation boundary condition was specified at the surface. The displacements in x, y, and z-directions, U_1, U_2, and U_3 respectively as well as the rotations in these directions, U_{R1}, U_{R2}, and U_{R3} respectively were set to 0 initially. However, U_3 was modified in the first Static step to a ramped displacement of magnitude 0.3mm and was propagated to the subsequent Visco step. Furthermore, a third boundary condition was applied at the crack which was constrained in the direction of application of the displacement; roller in z-direction. Since the created partition to represent the barb was defined as a crack, loads and boundary conditions could not be defined exactly at the surface. For this reason, a new partition was created by offsetting the plane of the crack by 0.005mm. The roller boundary condition was applied at that surface (Fig. 22).

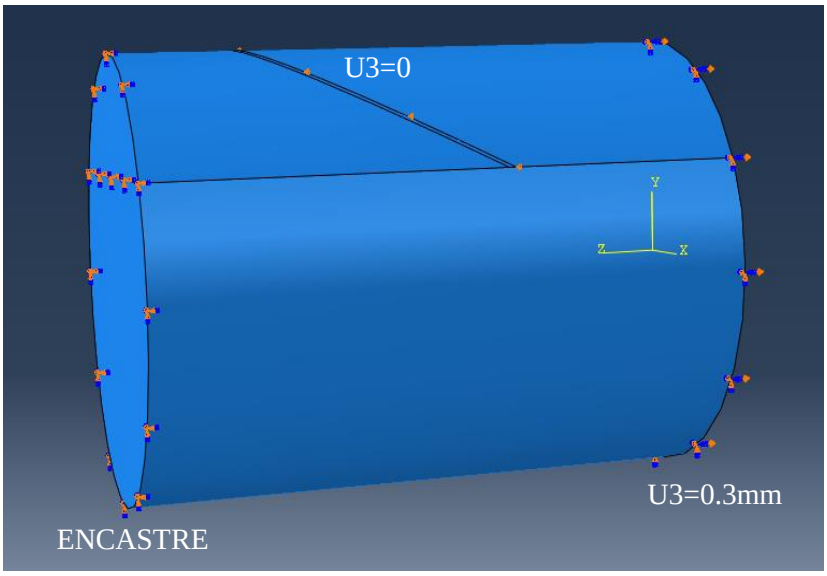

Figure 22: Boundary conditions for load case 2

Since the main concern from applying this test case is to investigate the strength of a single barb, average stresses at the surface of the crack were monitored at the onset of failure. For this reason, an element set, BabrElem, was created and associated with a Field Output Request to report Von-mises stresses. Figure 23 shows the location of BarbElem in a circular suture.

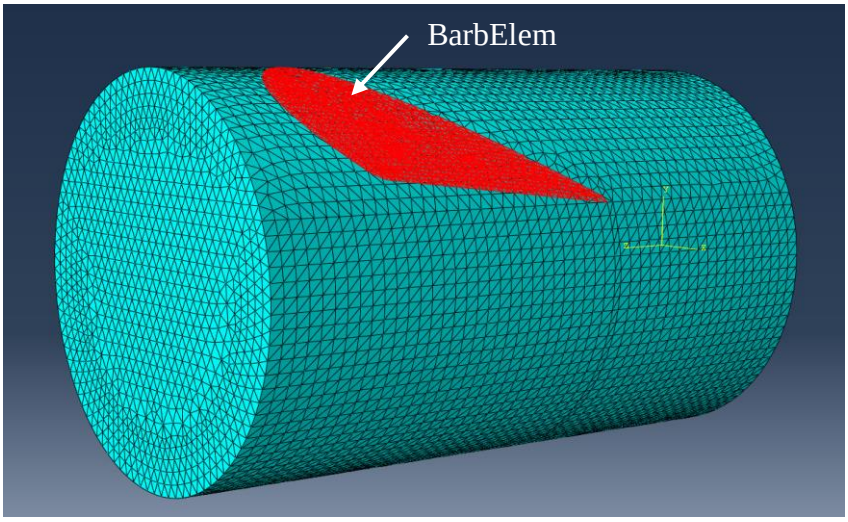

Figure 23: The position of BarbElem set highlighted in red

4.5.3. Loading Case 3

In order to investigate the behavior of the suture when loads are applied to both, the body of the suture and the surface of the barb, a third test case which combines the former test conditions was applied. The significance of this study lies in its resemblance to the real-life suture-tendon interaction. These loading conditions were considered for the final optimized geometry only.

4.5.3.1. Tendon Forces

To be able to mimic the real application, the load applied to the suture should be equal to those generated by a tendon during different rehabilitation exercises. Early tendon mobilization has been shown to facilitate tendon gliding and healing while reducing adhesion formation [65]. Three different schools of early rehabilitation programs exist [66]. The first recommends early passive mobilization combined with either actively extending-passively flexing the treated fingers or passively flexing and

extending. The second consists of passive flexion of the involved fingers that are then kept flexed actively. The last program favors early active mobilization where the treated fingers undergo active flexing. While active mobilization protocols are most of the time avoided for putting the repair at a higher risk of failure, rehabilitation programs that rely only on passive protocols expose the tendon to higher stakes of adhesion and the treated fingers to potential loss of range of motion. The most beneficial postoperative exercise protocol has not been agreed on yet. As a rule of thumb, finger motion during rehabilitation should generate forces that are high enough to induce tendon excursion but do not lead to gap formation or even, rupture.

Edsfeldt et al. recorded the peak forces exerted in the FDP and FDS tendons during five rehabilitation exercises for two different wrist positions: neutral and flexed (Fig. 24) [66]. The highest median forces were noted during isolated FDP and FDS flexions for both wrist positions. Magnitudes as high as 25N were observed for the FDP maneuver.

Forces recorded	Place and hold		Active finger flexion		Isolated FDP flexion		Isolated FDS flexion		Tenodesis
	Wrist neutral	Wrist flexed	Wrist neutral	Wrist flexed	Wrist neutral	Wrist flexed	Wrist neutral	Wrist flexed	
Peak FDP forces (N)									
Mean	3.6	3.1	6.5[a]	5.9	25.5[b]	23.8[b]	3.1	2.9	2.8
SD	3.1	2.8	5.1	4.7	20.4	19.6	5.2	7.5	4.8
Maximum	10.6	10.1	17.3	17.8	73.8	74.7	16.0	22.7	15.8
Peak FDS forces (N)									
Mean	4.9	7.7[c]	2.9	3.5	4.3	4.2	12.9[d]	14.1[d]	2.7
SD	2.6	5.6	6.7	12.9	3.1	5.1	6.4	8.0	1.0
Maximum	10.9	23.7	25.6	47.5	12.9	20.0	24.2	32.9	4.6

Figure 24: Peak forces recorded in FDP and FDS tendons during five rehabilitation exercises for two different wrist positions [66]

Although such flexion exercises should be avoided or applied with caution especially during the first 3 weeks after the repair surgery, a force of 25N was chosen as the tendon load to be applied in the model.

Furthermore, the repair should be still able to withstand the forces produced during early mobilization after tendon softening has occurred. For this reason, a factor of safety of 18% should be added to compensate for the decrease in repair strength. To account for gap formation, which hinders tendon retraction and may result in rupture, an extra 30% safety should be considered [66].

Taking into account all the safety factors, the 25N becomes 37N. It is reported in the literature that a suture with an ultimate strength of at least 30 to 55N is a must when gentle to moderate active rehabilitation maneuvers are involved [65]. As a result, a load of 40N was decided on to represent the forces generated by a tendon.

As such, for loading case 3, the left extremity was subjected to a displacement/rotation boundary condition. The displacements in x, y, and z-directions, U_1, U_2, and U_3 respectively as well as the rotations in these directions, U_{R1}, U_{R2}, and U_{R3} respectively were set to 0 initially. However, U_3 was modified in the first Static step to a ramped displacement of magnitude 0.096mm equivalent to 40N, as obtained from the load-displacement curve generated for the model on ABAQUS (Fig. 25). This value was propagated as a constant to the subsequent Visco step. The right extremity was fixed by an ENCASTRE boundary condition applied in the initial step and propagated to the following Static and Visco steps. Furthermore, a third boundary condition was applied at the crack. A ramped displacement of magnitude 0.05mm was defined perpendicular to the offset surface that was partitioned in the second test case (Fig. 26). This boundary

condition was created in the Visco step such that the body of the suture has been preloaded with a value of 40N.

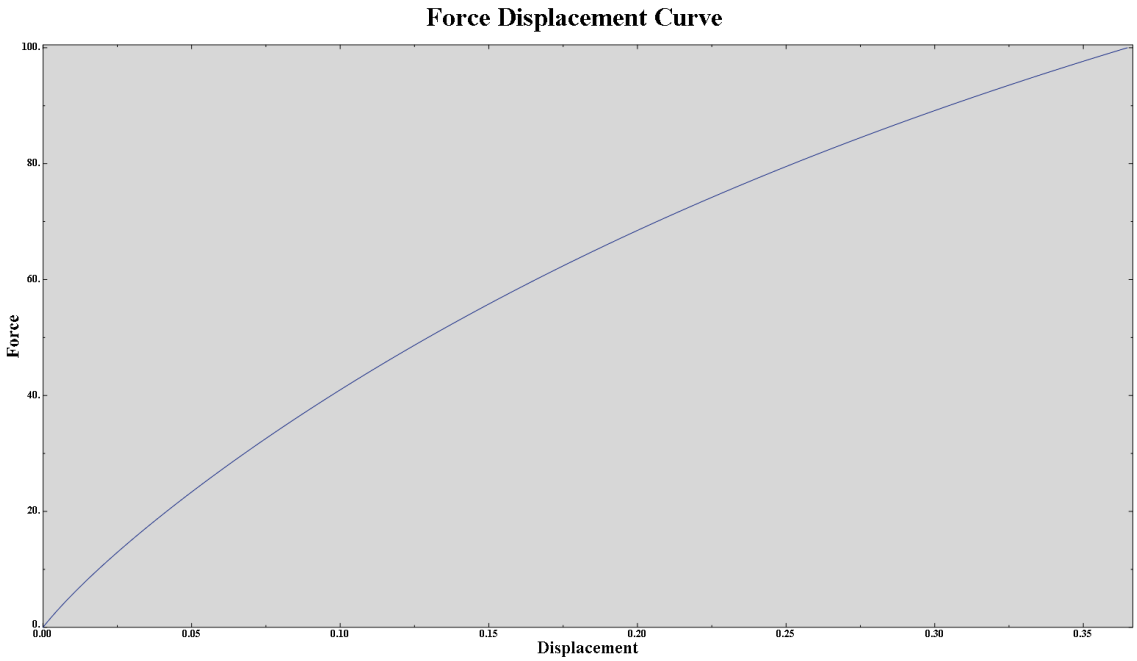

Figure 25: Force-Displacement curve as obtained from ABAQUS

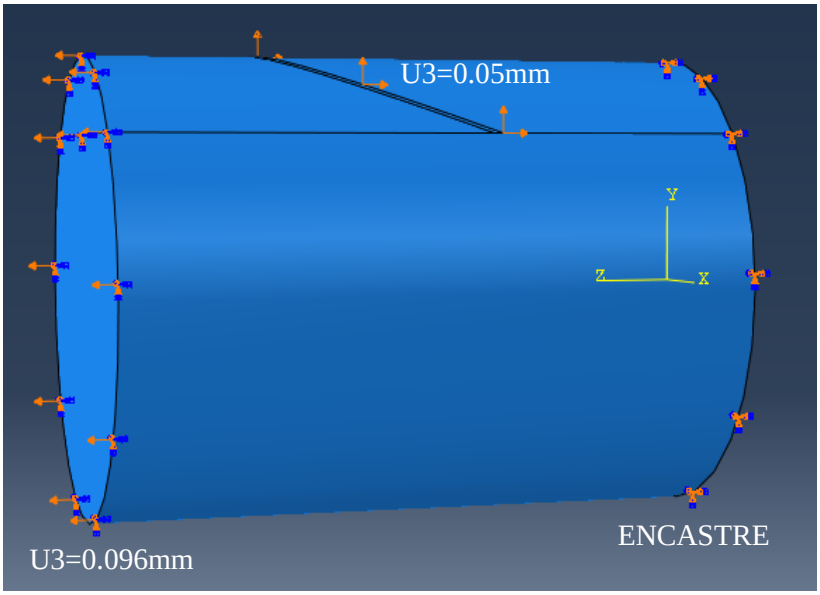

Figure 26: Boundary conditions for load case 3

The main motive behind running this test case was to determine the strength of a single barb when the whole suture was being loaded as well. For this reason, the average stresses at the surface of the crack were recorded at the onset of failure. The element set, BabrElem created in the second test case was used to report the average Von-mises stresses.

Once the force that a single barb can withstand before the onset of crack propagation is known, the number of barbs needed to be anchored in the tendon to support its action loads can be calculated. This number is approximately 40N divided by the force of a single barb.

4.6. Meshing

The impact of the quality of the mesh on the correctness of the generated solution can never be overemphasized. However, a high-quality mesh is not synonymous with a fine mesh. A judgment for a good mesh should be based on its ability to resolve the physics of the problem under study without adding unnecessary complications. Too many elements may result in long solver runs, and too few may lead to inaccurate results. Hence, a high-quality mesh is one that serves the objective of the model; obtain a solution with the needed accuracy by using only as many degrees of freedom as necessary.

In order to ensure that the generated mesh is of good quality, a trial and error analysis can be carried out. The mesh is refined until a critical result, such as the maximum stress in a specific location, converges; that is, it does not change significantly with further refinement (h-method).

A mesh convergence analysis was performed for this study for the two loading cases. The investigation was carried out for the circular suture ($\rho=1$) having a cut angle of 154°, and a cut depth 0.19mm.

4.6.1. Loading Case 1

The nature of the geometry at hand, a cylinder with a slanted cut, makes it difficult to use brick elements, even when extensive partitioning is performed. For this reason, meshing was done using linear tetrahedral elements (C3D4). A mesh sensitivity analysis was carried to determine the optimum mesh size among the tested values: 0.015, 0.02, 0.025, 0.027, 0.03, 0.031, 0.035, 0.037. The corresponding average strains at onset of failure for the set Elem1 for each mesh size are summarized in table 6. Figure 27 shows a plot of the failure strains with respect to the number of elements.

Mesh Convergence C3D4		
Mesh size	Number of Elements	Failure Strain (%)
0.015	376896	19.2
0.02	181649	17.76
0.025	98739	16.7
0.027	85062	24
0.03	60375	24.2
0.031	53559	18.74
0.035	40507	16.8
0.037	35679	16.82

Table 6: Average strains at failure (%) detected for different mesh sizes of linear tetrahedral elements

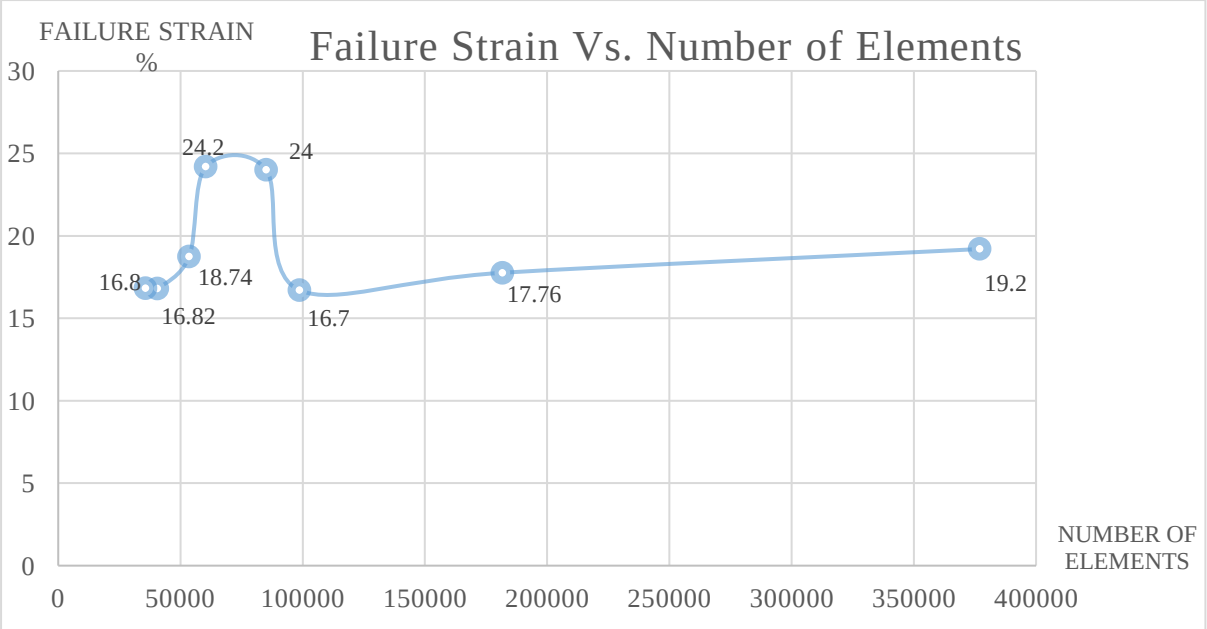

Figure 27: Average failure strain (%) versus number of elements in the mesh for the set Elem1

As evident from figure 27, no significant trend was observed and convergence was obviously not attained. An error of 31% between the maximum and minimum values of the strain was noted. To resolve this problem, a local structured mesh of brick elements with reduced integration (C3D8R) was generated in the critical region near the crack tip while keeping the global mesh type as tetrahedral elements C3D4 (Fig. 29).

Again, a mesh sensitivity analysis was performed for the mesh sizes: 0.015, 0.022, 0.024, 0.025, 0.027, 0.03, 0.035, 0.04, 0.05. For each mesh size, the corresponding average strain at onset of failure was recorded. The results are summarized in table 7. Figure 28 shows a plot of the failure strain with respect to the number of elements.

Mesh Convergence C3D8R		
Mesh size	Number of Elements	Failure Strain (%)
0.015	469222	19.45
0.022	174020	18.65
0.024	134521	17.8
0.025	124261	18
0.027	98441	18
0.03	80790	19.12
0.035	46826	20.3
0.04	32946	19.5
0.05	16527	18.8

Table 7: Average strains at failure (%) detected for different mesh sizes of mixed brick and tetrahedral elements

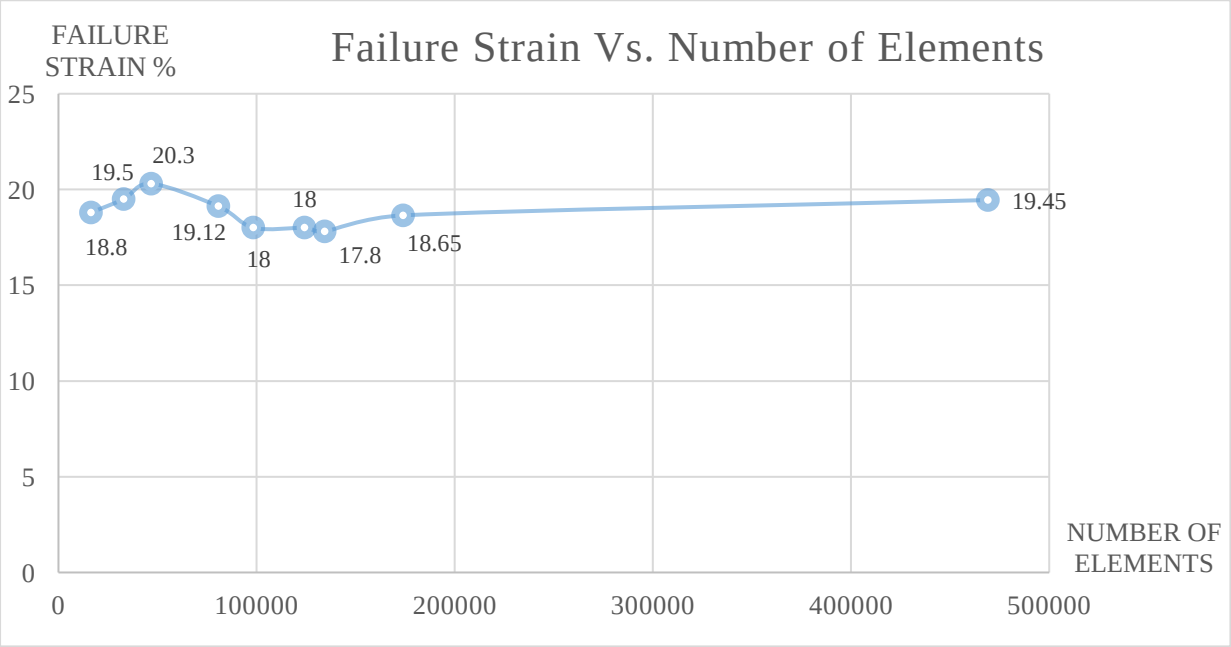

Figure 28: Average failure strain (%) versus number of elements for a mixed mesh for the set Elem1

Figure 28 reveals an evident trend for the average failure strain. As such, a converged mesh has been obtained with a maximum error of 12% between the maximum and minimum values of the strain. A mesh size of 0.025 (124261 elements) was chosen,

taking into consideration both accuracy of the results and the required simulation time. The final mesh is shown in figure 29 for a circular cross-section.

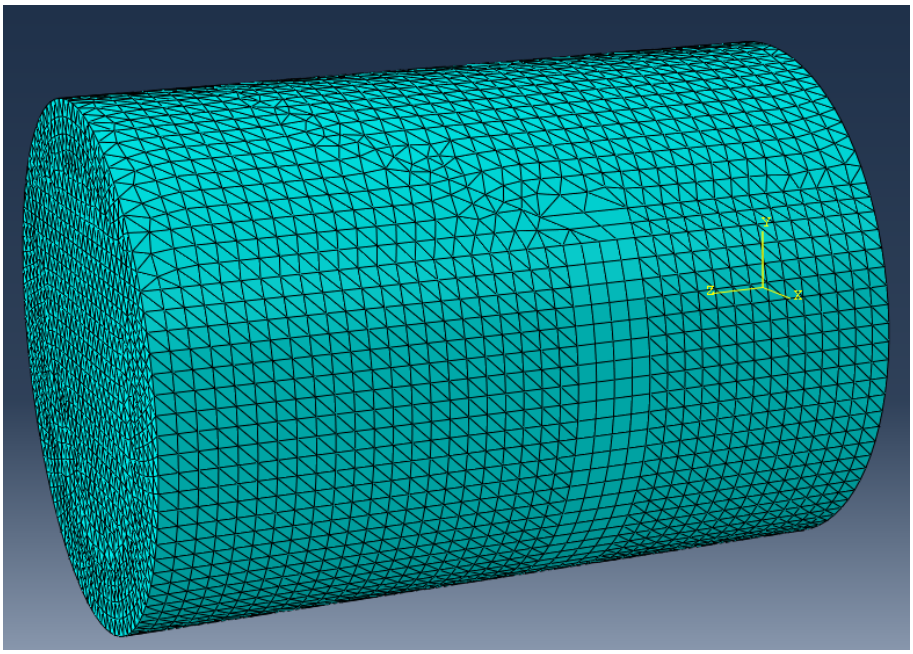

Figure 29: Mesh for load case 1 consisting of structured brick elements near the crack

4.6.2. Loading Case 2

When applying the mesh configuration that has been decided on as a result of the mesh convergence analysis performed for the first loading case, difficulties with reaching acceptable solutions were faced. When the crack was to propagate, nodes at the crack tip were being connected with ones facing them to form new elements instead of being deleted. For this reason, brick elements at the crack tip were found to be unsuitable with this type of analysis. Linear tetrahedral elements (C3D4) were used to mesh the whole model.

To decide on a mesh size, another mesh convergence study was carried out for this specific loading case. Mesh sizes of 0.02, 0.025, 0.03, and 0.035 were considered.

For each mesh size, the corresponding average maximum principal stress at the surface of the barb when a crack started to propagate (BarbElem) was recorded. The results are summarized in table 8. Figure 30 shows a plot of the maximum principle stress at failure with respect to the number of elements.

Mesh Convergence C3D4		
Mesh size	Number of Elements	Maximum Principal Stress (MPa)
0.02	183967	32.5
0.025	108708	29.9
0.03	66309	31.59
0.035	41139	32.5

Table 8: Average maximum principal stress (MPa) at failure detected for different mesh sizes of linear tetrahedral elements

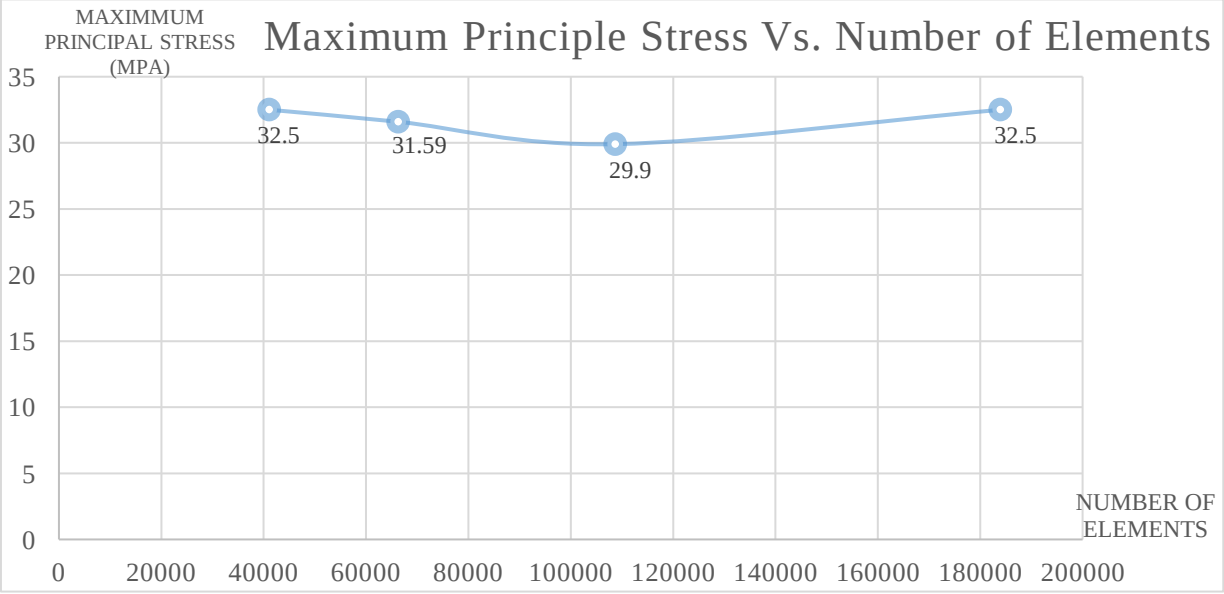

Figure 30: Average maximum principal stress (MPa) versus number of elements in the mesh for the set BarbElem

Figure 30 shows that a converged mesh has been attained with a maximum error of 8% between the maximum and minimum values of the maximum principal stress. For the same reasoning as in the first loading case, a mesh size of 0.025 (108708 elements) was chosen. The final mesh is shown in figure 31 for a circular cross-section.

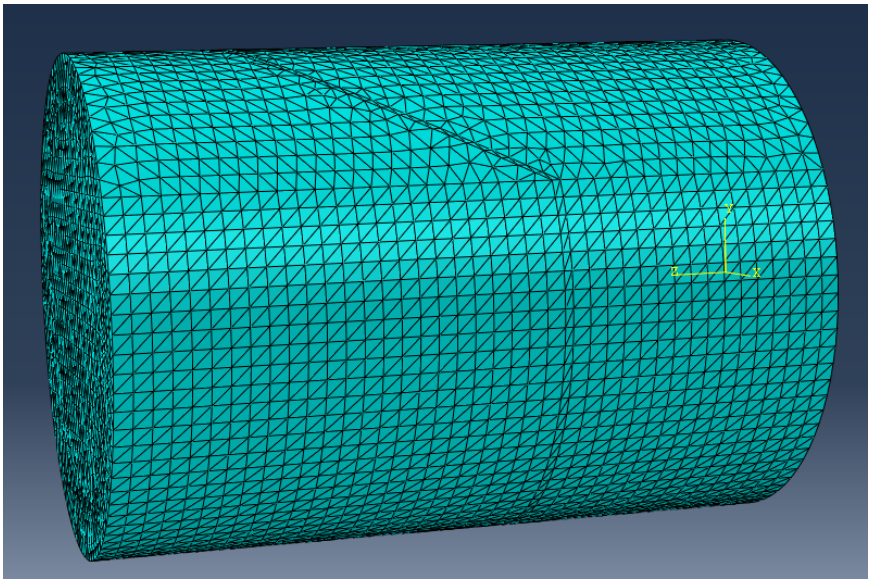

Figure 31: Mesh for load case 2 consisting of linear tetrahedral elements

CHAPTER 5

RESULTS

In this section, the finite element results of the models detailed above subjected to load cases 1 and 2 are reported. An optimized suture geometry is attained and tested under the third loading case.

At first, the aspect ratios were varied for a constant cross-sectional area equivalent to that of a circle having a radius of 0.3mm, a constant cut angle (CA) of 154° and cut depth (CD) of 0.19mm for both loading conditions. The second step was to investigate the effect of varying CA and CD for a constant ρ.

5.1. Constant Cut Angle and Cut Depth

5.1.1. Loading Case 1

An ENCASTRE and a displacement/rotation boundary conditions were applied to the suture geometry as thoroughly described in the Boundary Conditions and Loads section. Stresses and strains in the z-direction, S33 and NE33 respectively, in the body of the suture (Elem1) were reported at the onset of crack propagation and compared among the different cross-sections. The results are tabulated below (Table 9).

	Results for Load Case 1, constant CSA, CA=154°, CD=0.19mm	
	Elem 1	
Aspect Ratio (ρ)	NE33 (%)	S33 (MPa)
1/3	19.23	280
1/2	18.65	275.92
1	17.98	262
2	18.05	264
3	18.1	265

Table 9: Average stresses (MPa) and strains (%) at failure for load case 1, constant CSA, CA=154°, CD=0.19mm

It can be noted from table 9 that changing the aspect ratio affects the strength of the suture. The highest strains and stresses are observed for aspect ratio 1/3. As such, ρ=1/3 is the strongest, followed by 1/2, 3, 2, and finally 1. A circular suture is found to be the weakest among all configurations. However, since the differences in the magnitudes of NE33 and S33 are not significant, the results cannot be considered conclusive. No clear trend is detected.

Figure 32 depicts a propagating crack for a circular cross-section. The direction of propagation of the crack is almost perpendicular to the applied displacement. Rupture failure is spotted. Similar behaviors are observed for all other aspect ratios.

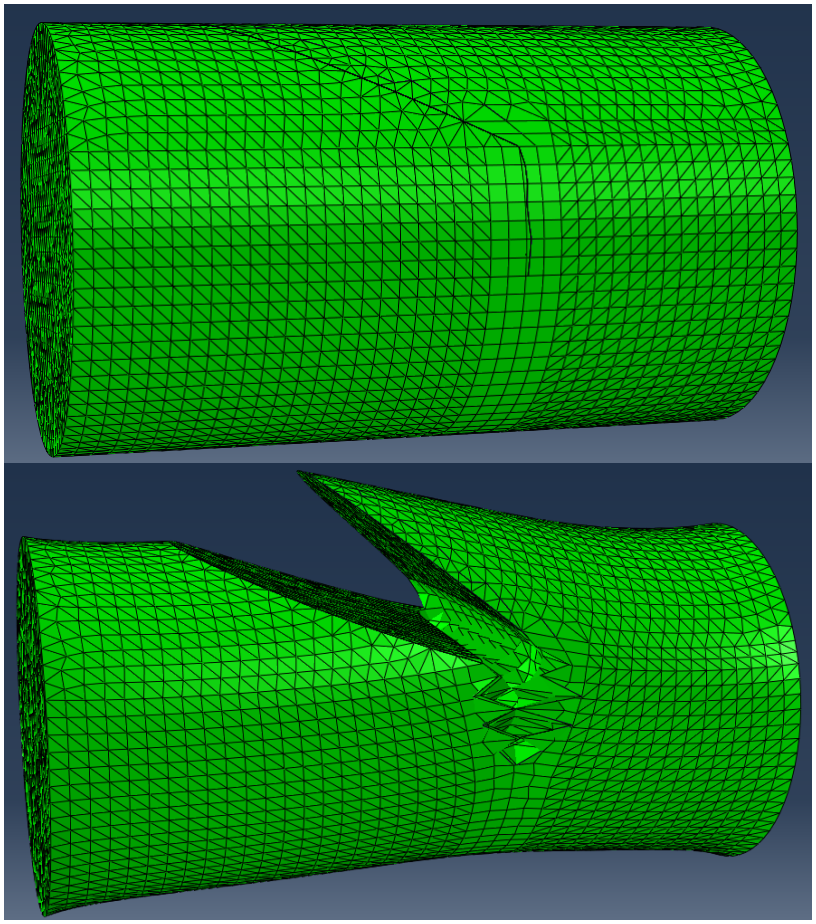

Figure 32: A propagating crack in a circular suture subjected to load case 1

5.1.2. Loading Case 2

An ENCASTRE and two displacement boundary conditions were applied as detailed in the Boundary Conditions and Loads section. Average von-mises stresses at the surface of the barb (BarbElem) were reported at the onset of crack propagation. The stresses were then converted into forces by multiplying them by the area of the barb. It was assumed that a barb is half an ellipse whose area is $(A)_{barb} = \pi ab/2$. The results are summarized in table 10.

	Results for Load Case 2, constant CSA, CA=154°, CD=0.19mm				
	Barb Area (mm^2)			BarbElem	
Aspect Ratio (ρ)	a (mm)	b (mm)	Area (mm^2)	Von-mises (MPa)	Force (N)
1/3	0.48343	0.250245	0.19	49	9.31
1/2	0.39474	0.306407	0.19	45.09	8.57
1	0.27911	0.433423	0.19	39.25	7.46
2	0.19732	0.612951	0.19	36	6.84
3	0.16115	0.750711	0.19	34.5	6.56

Table 10: Average stresses (MPa) and their corresponding forces at failure for load case 2, constant CSA, CA=154°, CD=0.19mm

The results in table 10 reveal an evident trend. As the aspect ratio decreases below 1, the barb strength increases. The opposite is noticed for increasing the aspect ratio beyond 1. Therefore, the strongest geometry belongs to ρ = 1/3, followed by 1/2, 1, 2, and finally 3. Notice that the area of the barb remains constant despite the variations in both major and minor axes of the ellipses. This is anticipated since the criterion for determining the dimensions of the ellipses was to have the same remaining area, or alternatively, equal areas removed.

Figure 33 shows the direction of propagation of the crack for a circular cross-section as being almost parallel to the applied displacement. Under such boundary conditions, peeling rather than rupture failure is detected. All other aspect ratios behave in a similar manner.

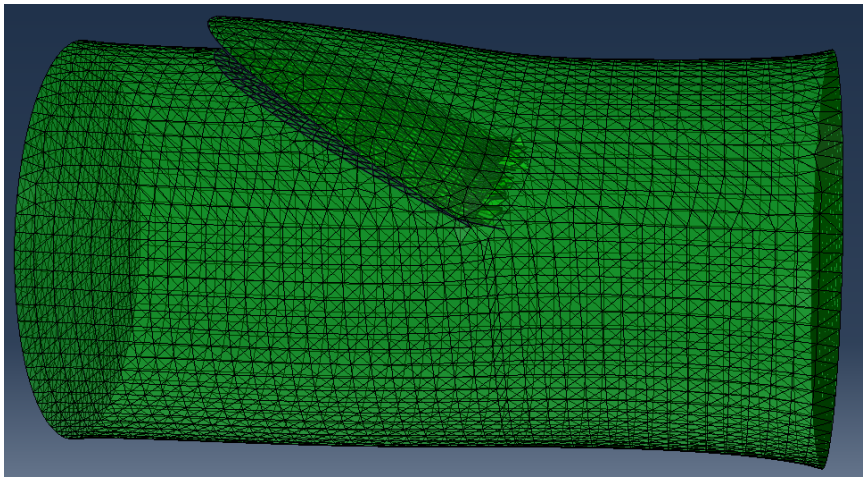

Figure 33: A propagating crack in a circular suture subjected to load case 2

The results for constant cross-sectional area, cut angle and cut depth for both load cases are summarized in figure 34. Percentage stains (%NE33) for LC1 and forces on the barb surfaces in Newtons (F-N) for LC2 are plotted. As aforementioned, based on LC1, a decisive conclusion regarding the best cross-sectional configuration cannot be made. A mere 7% increase in %NE33 is observed when comparing the weakest suture (ρ =1) with the strongest one (ρ = 1/3). Also, it is not clear which condition leads to an increased suture strength; decreasing the aspect ratio below one or increasing it. On the other hand, a 30% rise in the barb force is detected for LC2 when changing the aspect ratio from 3 to 1/3.

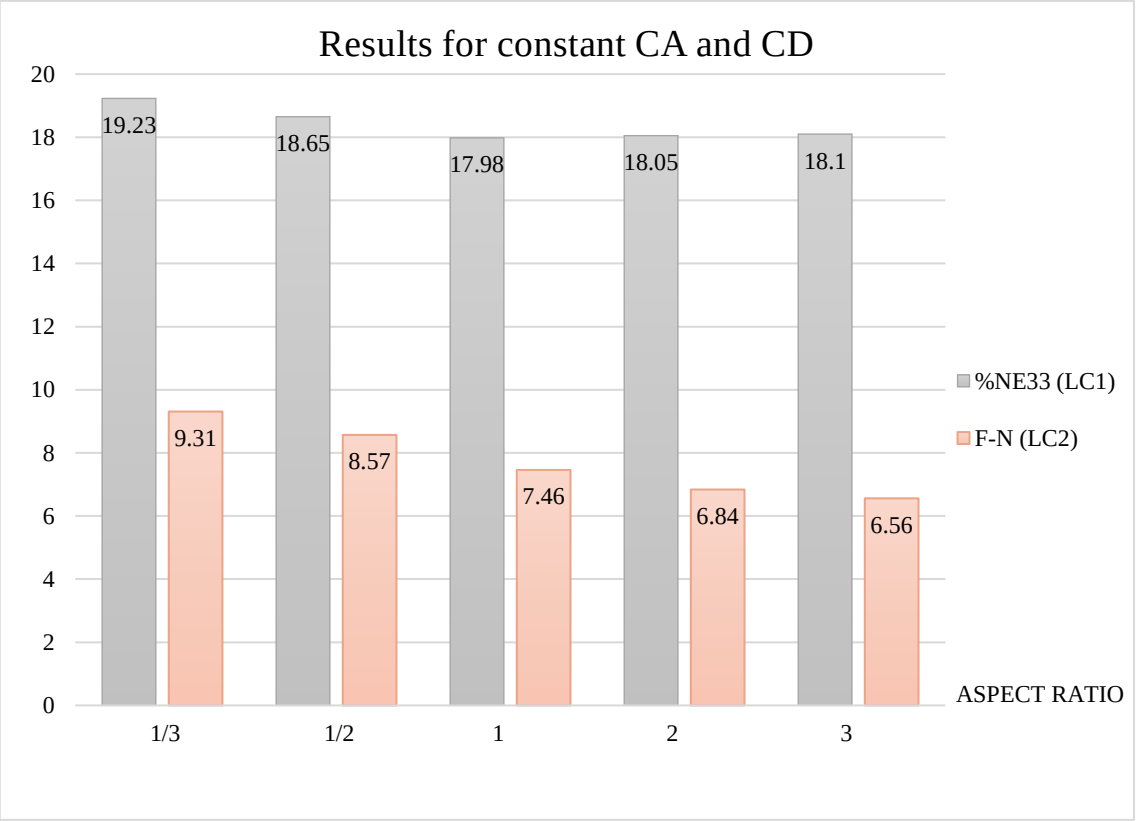

Figure 34: Summary of the results obtained for constant CA and CD for cases 1 and 2

Since on average, the aspect ratio ρ of the tendon is 2, a suture with an aspect ratio of 1/2, given the findings up till this point, appears to be most suitable. Furthermore, since the smallest major and minor axes among the tendons are a=1.5mm and b=0.858mm respectively, the radius (or the equivalent ellipse axes) of the suture can be increased from 0.3mm to a larger diameter that is suitable with both the dimensions of the smallest tendon and the optimum aspect ratio. It is desired that the optimized suture accommodates about 30% of the tendon's cross-sectional area. Consequently, a suggested geometry has the following characteristics: ρ =1/2, a=0.25mm and b=0.5mm.

5.2. Constant Aspect Ratio

For a constant ρ, the influence of varying CA and CD on the strength of the suture was studied. A circular cross-section was used with a radius of 0.3536mm equivalent to an ellipse having a=0.25mm and b=0.5mm. While the cut angles remain the same, the cut depths were adapted for the ellipse. The circle/ellipse equivalence for the newly proposed suture cross-section are listed in table 11.

		Ellipse Equivalence	
		Aspect Ratio	
		1/2	1
	Major axis a (mm)	0.25	0.3536
	Minor axis b (mm)	0.5	0.3536
	Cross-sectional Area (CSA) (mm^2)	0.3928	0.3928
CD = 0.07 mm	Remaining Area (RA) (mm^2)	0.3726	0.3726
	Cut distance d (mm)	0.2005	0.2836
	Cut depth (mm)	0.0495	0.07
CD = 0.12 mm	Remaining Area (RA) (mm^2)	0.3485	0.3485
	Cut distance d (mm)	0.16515	0.2336
	Cut depth (mm)	0.0849	0.12
CD = 0.19 mm	Remaining Area (RA) (mm^2)	0.3078	0.3078
	Cut distance d (mm)	0.11565	0.1636
	Cut depth (mm)	0.1344	0.19

Table 11: Equivalent dimensions and cut depths for ρ = 1/2

5.2.1. Loading Case 1

The boundary conditions associated with this load case were applied to a cylinder with a circular cross-section of r = 0.3536mm for the cut angles 150°, 154°, and 160°, and cut depths 0.07mm, 0.12mm, and 0.19mm. The outputs of interest are the same as before for the same load case. The obtained results are summarized in table 12.

		Results for Load Case 1, ρ = 1, r=0.3536mm	
		Elem 1	
Cut Angle (°)	Cut Depth (mm)	NE33 (%)	S33 (MPa)
160	0.19	21.55	306
	0.12	24	325
	0.07	29.63	384
154	0.19	18.1	264
	0.12	21.18	297
	0.07	26.25	350
150	0.19	17	250
	0.12	20.05	285
	0.07	25.06	336

Table 12: Average stresses (MPa) and strains (%) at failure for load case 1, ρ=1 for varying cut angles and cut depths

For a constant cut angle, decreasing the cut depth leads to stronger sutures that fracture at higher average strains. This result is expected since a smaller cut depth is synonymous with a smaller crack. On the other hand, for a constant cut depth, increasing the cut angle results in stronger geometries. From this analysis, the best configuration is CA=160° and CD=0.07mm.

5.2.2. Loading Case 2

The analysis was performed for a circular suture of r = 0.3536mm for the cut angles and cut depths 150°, 154°, and 160°, and 0.07mm, 0.12mm, and 0.19mm respectively. The outputs of interest are the same as before for the same load case. The obtained results are summarized in table 13.

		Results for Load Case 2, ρ = 1, r=0.3536mm				
		Barb Area (mm^2)			BarbElem	
Cut Angle (°)	Cut Depth (mm)	a (mm)	b (mm)	Area (mm^2)	Von-mises (MPa)	Force (N)
160	0.19	0.313477	0.555523	0.2735	37.76	10.33
	0.12	0.265451	0.350857	0.1463	47.39	6.93
	0.07	0.211197	0.204666	0.0679	54.9	3.73
154	0.19	0.313477	0.433423	0.2134	39.08	8.34
	0.12	0.265451	0.273741	0.11414	41.22	4.7
	0.07	0.211197	0.159682	0.053	56.9	3.02
150	0.19	0.313477	0.38	0.18712	36.035	6.74
	0.12	0.265451	0.24	0.1	43.68	4.368
	0.07	0.211197	0.14	0.0464	58.42	2.71

Table 13: Average stresses (MPa) and their corresponding forces at failure for load case 2, ρ=1 for varying cut angles and cut depths

For a constant cut angle, decreasing the cut depth results in a weaker barb that can withstand lower forces. On the other hand, for a constant cut depth, increasing the cut angle results in stronger barbs. This is expected, for when both CA and CD increase, the barb area increases as well, as evident in table 13, allowing it to endure higher forces. From this analysis, the best configuration is CA=160° and CD=0.19mm.

The results for a constant aspect ratio are plotted in figure 35. Percentage stains (%NE33) for LC1 and forces on the barb surfaces in Newtons (F-N) for LC2 are summarized. A cut angle of 160° shows evident superiority over other values considered for both load cases. For a constant cut depth of 0.19mm, an increase of 27% in %NE33 and 53% in barb force is detected when comparing CA 150° to 154°. However, detecting a prominent cut depth is not as straightforward as that for a cut angle. For a constant CA of 160°, a decrease of 27% was observed for an increase in CD from 0.07mm to 0.19mm

under LC1. For LC2, the opposite is observed, where the same increase in CD leads to a higher barb force by 177%.

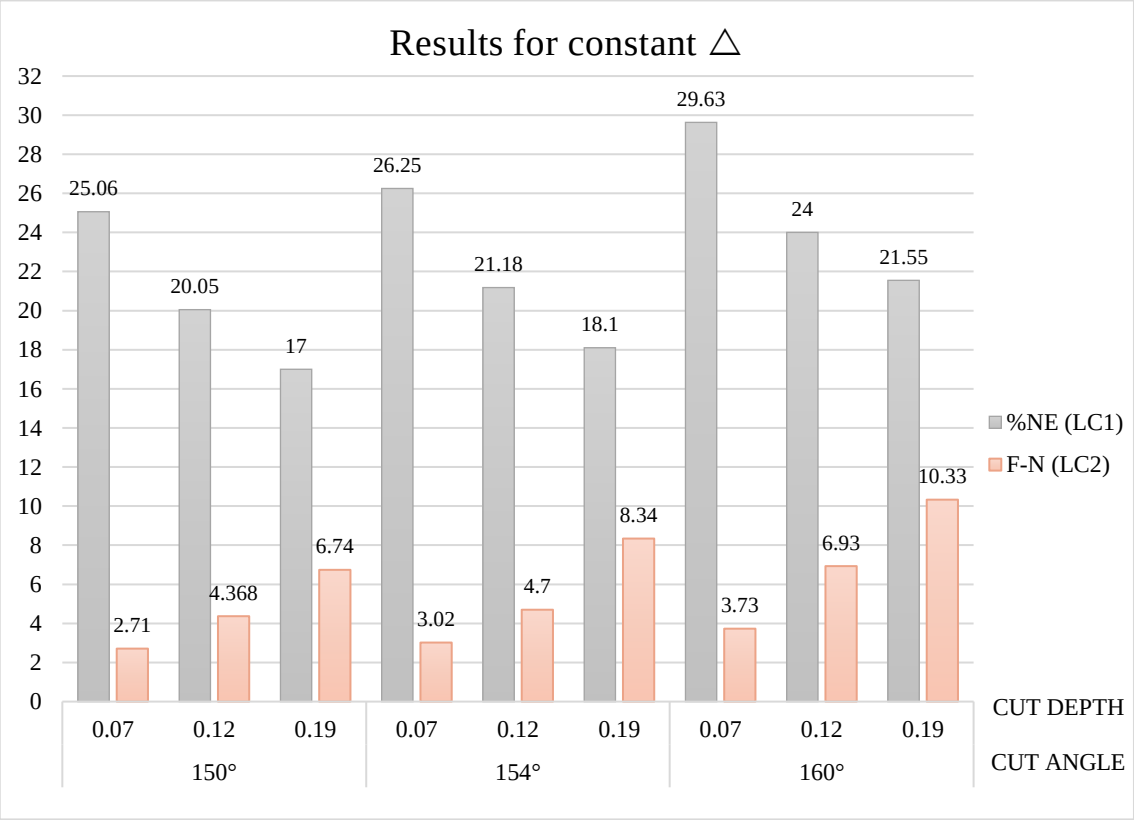

Figure 35: Summary of the results obtained for constant aspect ratio under both load cases 1 and 2

5.3. Optimized Geometry

With respect to aspect ratios, it was concluded that ρ = 1/3 presents the strongest design as compared to other aspect ratios. Taking into consideration the tendon's cross-section, it was decided that ρ = 1/2 is most suitable.

Concerning cut angles and cut depths, it was found from the first load case that the best configuration corresponds to CA=160° and CD=0.07mm. For the second test case, CA=160° and CD=0.19mm were found to offer the best results. As such, a cut angle

of 160° is evidently superior. However, a decision on the cut angle is not direct. A middle value between 0.19mm and 0.07mm was chosen; that is, 0.12mm.

Therefore, the optimum geometry has an aspect ratio ρ =1/2, CA=160° and CD=0.12mm. Load cases 1 and 2 were performed again for this optimized geometry. The results are reported in table 14.

Results for ρ= 1/2, CA=160°, CD=0.12mm			
Loading Case 1		Loading Case 2	
Elem 1		BarbElem	
NE33 (%)	S33 (MPa)	Von-mises (MPa)	Force (N)
26.88	362	52.69	7.71

Table 14: Results for the optimized geometry for load cases 1 and 2

Comparing the results with those obtained for a circular cross-section (Table 15) for the same cut angle and cut depth confirms the conclusion that aspect ratio 1/2 is superior. The average strains as well as the forces at the surface of the barb at onset of crack propagation increase by 12%, and 11% respectively.

Results for ρ= 1, CA=160°, CD=0.12mm			
Loading Case 1		Loading Case 2	
Elem 1		BarbElem	
NE33 (%)	S33 (MPa)	Von-mises (MPa)	Force (N)
24	325	47.39	6.93

Table 15: Results for ρ= 1, CA=160°, CD=0.12mm subjected to both load cases 1 and 2

Since the values for both cut angle and cut depth were varied for a circular cross-section, the observed trend was to be validated for ρ = 1/2. The test was performed once for a

constant CA of 160° and two different values for CD: 0.19mm and 0.12mm, and another time for a constant CD of 0.19mm while changing the CA from 160° to 154°.

The obtained results are summarized in table 16. For a constant cut depth, decreasing the cut angle resulted in a weaker suture and a barb that can tolerate lower forces (decrease of 14% in %NE33 and 33% in the force), as observed for ρ=1. For a constant cut angle, decreasing the cut depth resulted in a stronger suture (24% higher %NE33) but a weaker barb (120% lower barb forces). This was also noted for a circular cross-section.

		Loading Case 1		Loading Case 2	
		Results for ρ= 1/2, a=0.25mm, b=0.5mm			
		Elem 1		BarbElem	
Cut Angle (°)	Cut Depth (mm)	NE33 (%)	S33 (MPa)	Von-mises (MPa)	Force (N)
160	0.19	21.71	311	61.9	16.93
	0.12	26.88	362	52.69	7.71
154	0.19	18.7	275	52.8	11.27
		Results for ρ= 1, r=0.3536mm			
160	0.19	21.55	306	37.76	10.33
	0.12	24	325	47.39	6.93
154	0.19	18.1	264	39.08	8.34

Table 16: Summary of results for ρ=1 and ρ=1/2, for varying cut angles and cut depths under both load cases

5.3.1. Loading Case 3

This loading case was performed for the optimized cut angle of 160°and cut depth of 0.12mm, but for ρ=1, since generating a working mesh for ρ=1/2 was problematic under the prescribed boundary conditions.

Reporting the findings for this test case, a small difference was noticed in comparison with the second loading condition. A force of 6.26N was obtained as opposed to 6.93N (10% difference). The same trend is expected for ρ=1/2 but most likely, the percent variation differs. However, this decrease in barb strength would be accounted for in safety factors when determining the number of barbs required to be anchored within the tendon. The results are tabulated below (Table 17).

Results for ρ= 1, CA=160°, CD=0.12mm	
Loading Case 3	
BarbElem	
Von-mises (MPa)	Force (N)
42.8	6.26
Loading Case 2	
47.39	6.93

Table 17: Results for optimized cut angle and cut depth for ρ=1 for load cases 2 and 3

5.3.1.1. Number of Barbs Required

As aforementioned, an estimation of the number of barbs required to hold a tendon force equivalent to 40N can be simply found by dividing this force by the one withstood by a single barb.

For ρ=1/2, CA= 160°, CD=0.12mm, the force at the barb surface was recorded to be 7.71N. This value represents the force at which crack propagation initiates. Certainly, the barb should be loaded at forces lower than the threshold. And since for the third loading case, a value lower than 7.71 is anticipated, the force at the barb surface is assumed to be 5N, 35% less. Taking into consideration a factor of safety of 3, the required number of barbs to be anchored in the tendon to withstand 40N becomes:

$$\text{Number of barbs} = \frac{(40)(3)}{(5)} = 24 \text{ Barbs}$$

Hence, 24 barbs are required. Note that this number is a mere estimate. A method to obtain a more accurate number is suggested in the *"Future Work"* section.

CHAPTER 6

DISCUSSION

In this section, the mechanisms that led to the obtained results are discussed. The outcomes of the finite element analysis are not accepted at face value.

6.1 Constant Cut Angle and Cut Depth

For a constant cut angle and cut depth, it was noticed that decreasing the aspect ratio below ρ=1 resulted in stronger sutures, or more accurately, barbs. For this case, since the remaining areas of the ellipses are the same, the only variables are the cut length $\left(CL = CD/\sin(180 - CA)\right)$ and the crack length (Fig. 36). As the aspect ratio increases from 1/3 to 3, the cut length, which is also equal to the minor axis "b" of the elliptical barb, increases as well, while the crack length, twice the major axis "2a" of the barb, decreases proportionally (Table 13).

With this in mind, we suspect that the main reason behind the observed results is the stress intensity factor. For Modes I and II, $K_I = \sigma\sqrt{\pi a}F_I(a/W)$ and $K_{II} = \tau\sqrt{\pi a}F_{II}(a/W)$ respectively, where σ, τ are the characteristic stresses in the part, a is the crack length, W is the width of the part, and F_I, F_{II} are functions of the ratio of the crack length to the width of the specimen and the type of the load being applied. Contours of stress intensity factors for a stationary crack were plotted on ABAQUS. The average values are reported in Table 18.

	Stress Intensity Factors		
Aspect Ratio	KI ($MPa\sqrt{m}$)	KII ($MPa\sqrt{m}$)	KIII ($MPa\sqrt{m}$)
1/3	105	-122	-4.11
1/2	106	-119	-1.6
1	57.7	-79.5	-1.14
2	79.4	-120	2.34
3	66.3	-124	-0.484

Table 18: Stress intensity factors for Modes I, II, and II

It is evident that mixed-mode crack growth takes place with a slight Mode II dominance. The observed trend for varying the aspect ratio is a result of the combination of the three Modes, governed by the mixed-mode power law (Eq. 34). The resultant stress intensity factor, or more specifically, energy release rate is suspected to be highest for ρ=3 followed by 2, 1, 1/2 and finally 1/3. This explains the decrease in suture/barb strength as the aspect ratio is varied from 1/3 to 3.

6.2 Constant Aspect Ratio

For a constant aspect ratio, two opposing behaviors were noted. A stronger suture is obtained for a decreasing cut depth but an increasing cut angle. However, with respect to barb strength, an increase in both cut angle and cut depth enhanced the performance of the barb.

Considering the first case, for a constant cut angle, decreasing the cut depth means that the crack size has been reduced (smaller barb), leading to an increased strength of the body of the suture. As for a constant cut depth, the increase in cut angle results in a longer cut length (CL), which can be observed as the moment arm that translates the

forces at the barb surface into compressive stresses at the crack tip (Fig. 36). The higher the compressive stresses, the more opposition there is to crack growth, and the stronger the suture is.

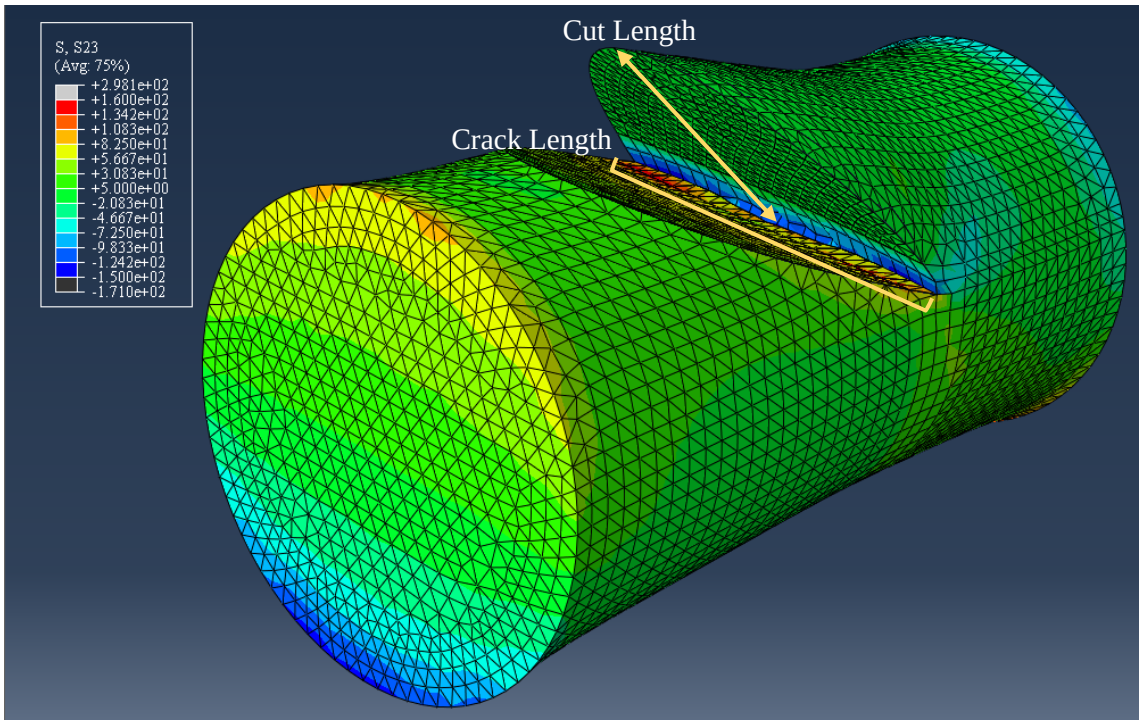

Figure 36: Plot of shear stresses (S23) for ρ= 1, CA=154°, CD=0.19mm for load case 1. Notice the initiation of crack propagation mid crack length.

For the second case, the logic is more straightforward. Increasing both the cut angle and cut depth lead to larger barb areas that can tolerate higher forces.

CHAPTER 7

CONCLUSION AND FUTURE WORK

7.1 Conclusion

In this work, the extended finite element method (XFEM) has been successfully implemented on ABAQUS to predict crack growth in viscoelastic material. The aim was to employ this technique as a tool to assess the mechanical performance of barbed sutures for use in flexor tendon repair and ultimately suggest a new optimized suture geometry for a novel single-stranded repair technique.

Inspired by the geometry of flexor tendons, an elliptical suture cross-section was investigated. Two other geometrical factors were varied: cut angle and cut depth. In total, five different aspect ratios (ρ= 1/3, 1/2, 1, 2, 3), three different cut angles (150°, 154°, 160°) and three different cut depths (0.07mm, 0.12mm, 0.18mm) were studied for two different loading conditions; one to assess the strength of the suture, the second to evaluate the strength of a single barb.

The results revealed that for a constant cut angle and cut depth, decreasing the aspect ratio below ρ=1 resulted in stronger sutures and barbs. For a constant aspect ratio, the strength of the suture was improved for lower cut depths but higher cut angles. However, with respect to the barb, an increase in both cut angle and cut depth enhanced its performance.

Based on the results, an elliptical suture having an aspect ratio 1/2, cut angle 160°, and cut depth 0.12mm is recommended with 24 barbs anchored into the tendon.

7.2 Future Work

Without doubt, the outcome of this work presents a solid foundation towards the use of a new barbed suture design for a novel single-stranded repair technique. For a more comprehensive assessment, the following points are suggested for future work:

- In this study, the suture material was taken as polypropylene. A material that has superior mechanical properties, for example polyglyconate, can be considered to further enhance the suture strength.
- The analysis here was performed for the properties of polypropylene at room temperature. Since sutures are used inside the human body, temperature effects on their performance should be studied.
- An experimental validation for the optimized geometry reached can be conducted to confirm with the results of the finite element analysis.
- The number of barbs required to be anchored in the tendon can be calculated more accurately taking into consideration that not all barbs will carry the same load (exponential decrease for example). Also, the length of the stitch that is allowed to be made in the tendon should be taken into account.
- A single barb was modelled here. Multiple barbs can be considered in order to understand how they interact with each other to decide on a distance between them and/or an angle of spirality.
- The barb and the suture, throughout this analysis, met in a straight line (crack edge) that traversed the suture from edge to edge. The effect of changing the length of this crack edge and/or its shape on barb performance could be considered.

REFERENCES

1. McClellan, W.T., et al., *A knotless flexor tendon repair technique using a bidirectional barbed suture: an ex vivo comparison of three methods.* Plastic and reconstructive surgery, 2011. **128**(4): p. 322e-327e.
2. Shah, A., M. Rowlands, and A. Au, *Barbed Sutures and Tendon Repair—a Review.* HAND, 2015. **10**(1): p. 6-15.
3. Strickland, J.W., *Development of flexor tendon surgery: twenty-five years of progress.* The Journal of hand surgery, 2000. **25**(2): p. 214-235.
4. Jordan, M.C., et al., *Suture material for flexor tendon repair: 3-0 V-Loc versus 3-0 Stratafix in a biomechanical comparison ex vivo.* Journal of orthopaedic surgery and research, 2014. **9**(1): p. 1.
5. Gussous, Y.M., et al., *The resurgence of barbed suture and connecting devices for use in flexor tendon tenorrhaphy.* HAND, 2011. **6**(3): p. 268-275.
6. Joyce, C.W., et al., *A barbed suture repair for flexor tendons: a novel technique with no exposed barbs.* Plastic and Reconstructive Surgery Global Open, 2014. **2**(10).
7. Naleway, S.E., et al., *Mechanical properties of suture materials in general and cutaneous surgery.* Journal of Biomedical Materials Research Part B: Applied Biomaterials, 2015. **103**(4): p. 735-742.
8. Viinikainen, A., et al., *A comparative analysis of the biomechanical behaviour of five flexor tendon core sutures.* The Journal of Hand Surgery: British & European Volume, 2004. **29**(6): p. 536-543.
9. Parikh, P.M., S.P. Davison, and J.P. Higgins, *Barbed suture tenorrhaphy: an ex vivo biomechanical analysis.* Plastic and reconstructive surgery, 2009. **124**(5): p. 1551-1558.
10. Rawson, S., S. Cartmell, and J. Wong, *Suture techniques for tendon repair; a comparative review.* Muscles, ligaments and tendons journal, 2013. **3**(3): p. 220.
11. Kanz, B.N., et al., *Biomechanical evaluation of a knotless barbed suture repair in a human Achilles tendon rupture model.* Foot & ankle specialist, 2014. **7**(3): p. 176-181.
12. Marrero-Amadeo, I.C., et al., *Flexor tendon repair with a knotless barbed suture: a comparative biomechanical study.* The Journal of hand surgery, 2011. **36**(7): p. 1204-1208.
13. Ingle, N.P., *Prototyping and Finite Element Analysis of Tissue Specific Barbed Sutures.* 2009.
14. Lin, T.E., et al., *Biomechanical analysis of knotless flexor tendon repair using large-diameter unidirection barbed suture.* Hand, 2013. **8**(3): p. 315-319.
15. Vizesi, F., et al., *Stress relaxation and creep: viscoelastic properties of common suture materials used for flexor tendon repair.* The Journal of hand surgery, 2008. **33**(2): p. 241-246.
16. Von Fraunhofer, J., et al., *Tensile strength of suture materials.* Journal of biomedical materials research, 1985. **19**(5): p. 595-600.
17. Von Fraunhofer, J., R. Storey, and B. Masterson, *Tensile properties of suture materials.* Biomaterials, 1988. **9**(4): p. 324-327.
18. Greenwald, D., et al., *Mechanical comparison of 10 suture materials before and after in vivo incubation.* Journal of surgical research, 1994. **56**(4): p. 372-377.
19. Ingle, N. and M. King, *Optimizing the tissue anchoring performance of barbed sutures in skin and tendon tissues.* Journal of biomechanics, 2010. **43**(2): p. 302-309.
20. Ingle, N.P., *Mechanical Performance and Finite Element Analysis of Bi-directional Barbed Sutures.* 2004.
21. Peltz, T., et al., *Performance of a knotless four-strand flexor tendon repair with a unidirectional barbed suture device: a dynamic ex vivo comparison.* Journal of Hand Surgery (European Volume), 2013: p. 1753193413476607.

22. Ingle, N., M. King, and M. Zikry, *Finite element analysis of barbed sutures in skin and tendon tissues.* Journal of biomechanics, 2010. **43**(5): p. 879-886.
23. Zeplin, P.H., et al., *Biomechanical evaluation of flexor tendon repair using barbed suture material: a comparative ex vivo study.* The Journal of hand surgery, 2011. **36**(3): p. 446-449.
24. Trail, I., E. Powell, and J. Noble, *An evaluation of suture materials used in tendon surgery.* Journal of Hand Surgery (British and European Volume), 1989. **14**(4): p. 422-427.
25. Dennis, C., et al., *Suture materials — Current and emerging trends.* Journal of Biomedical Materials Research Part A, 2016. **104**(6): p. 1544-1559.
26. Vincent, J.F., *Structural biomaterials*. 2012: Princeton University Press.
27. Drabousky, D.P., *Prony series representation and interconversion of viscoelastic material functions of equine cortical bone*. 2009, Case Western Reserve University.
28. Tzikang, C., *Determining a Prony series for a viscoelastic material from time varying strain data.* 2000.
29. Williams, J., *Visco-elastic and thermal effects on crack growth in PMMA.* International Journal of Fracture Mechanics, 1972. **8**(4): p. 393-401.
30. Williams, J., *Fracture mechanics of polymers.* Polymer Engineering & Science, 1977. **17**(3): p. 144-149.
31. Vincent, P. and K. Gotham, *Effect of Crack Propagation Velocity on the Fracture Surface Energy of Poly (methyl methacrylate).* 1966.
32. Kostrov, B. and L. Nikitin, *Some general problems of mechanics of brittle fracture(Brittle fracture mechanism models and connection with rheological properties of material, deriving relations for Griffith energy criterion).* Archiwum Mechaniki Stosowanej, 1970. **22**(6): p. 749-776.
33. Knauss, W., *Delayed failure—the Griffith problem for linearly viscoelastic materials.* International Journal of Fracture Mechanics, 1970. **6**(1): p. 7-20.
34. Knauss, W.G., *On the steady propagation of a crack in a viscoelastic sheet: experiments and analysis*, in *Deformation and Fracture of High Polymers*. 1973, Springer. p. 501-541.
35. Knauss, W., *Time dependent fracture and cohesive zones.* Journal of Engineering Materials and Technology, 1993. **115**(3): p. 262-267.
36. Schapery, R., *A theory of crack initiation and growth in viscoelastic media.* International Journal of Fracture, 1975. **11**(1): p. 141-159.
37. Schapery, R., *A theory of crack initiation and growth in viscoelastic media II. Approximate methods of analysis.* International Journal of Fracture, 1975. **11**(3): p. 369-388.
38. Schapery, R., *A theory of crack initiation and growth in viscoelastic media. III-Analysis of continuous growth.* International Journal of Fracture, 1975. **11**: p. 549-562.
39. Schapery, R., *A method for predicting crack growth in nonhomogeneous viscoelastic media.* International Journal of Fracture, 1978. **14**(3): p. 293-309.
40. McCartney, L., *Crack propagation, resulting from a monotonic increasing applied stress, in a linear viscoelastic material.* International Journal of Fracture, 1977. **13**(5): p. 641-654.
41. McCartney, L., *Crack propagation in linear viscoelastic solids: some new results.* International Journal of Fracture, 1978. **14**(6): p. 547-554.
42. Mc Cartney, L., *Crack growth laws for a variety of viscoelastic solids using energy and COD fracture criteria.* International Journal of Fracture, 1979. **15**(1): p. 31-40.
43. Christensen, R., *Lifetime predictions for polymers and composites under constant load.* Journal of Rheology (1978-present), 1981. **25**(5): p. 517-528.
44. Christensen, R. and R. Glaser, *The application of kinetic fracture mechanics to life prediction for polymeric materials.* Journal of applied mechanics, 1985. **52**(1): p. 1-5.

45. Marshall, G. and J. Williams, *The correlation of fracture data for PMMA.* Journal of Materials Science, 1973. **8**(1): p. 138-140.
46. Marshall, G., L.H. Coutts, and J. Williams, *Temperature effects in the fracture of PMMA.* Journal of Materials Science, 1974. **9**(9): p. 1409-1419.
47. Williams, J. and G. Marshall. *Environmental crack and craze growth phenomena in polymers*. in *Proceedings of the Royal Society of London A: Mathematical, Physical and Engineering Sciences*. 1975. The Royal Society.
48. Barenblatt, G.I., *The mathematical theory of equilibrium cracks in brittle fracture.* Advances in applied mechanics, 1962. **7**: p. 55-129.
49. Bradley, W., W. Cantwell, and H.H. Kausch, *Viscoelastic creep crack growth: a review of fracture mechanical analyses.* Mechanics of time-dependent materials, 1997. **1**(3): p. 241-268.
50. Frassine, R. and A. Pavan, *An application of viscoelastic fracture criteria to steady crack propagation in a polymeric material under fixed deformation.* International journal of fracture, 1990. **43**(4): p. 303-317.
51. Dubois, F., C. Chazal, and C. Petit, *Viscoelastic crack growth process in wood timbers: An approach by the finite element method for mode I fracture.* International journal of fracture, 2002. **113**(4): p. 367-388.
52. Dugdale, D.S., *Yielding of steel sheets containing slits.* Journal of the Mechanics and Physics of Solids, 1960. **8**(2): p. 100-104.
53. *ASTM C1557-14, Standard Test Method for Tensile Strength and Young's Modulus of Fibers*. 2014, ASTM International: West Conshohocken, PA.
54. SIMULIA, A., *6.12-1.* ABAQUS Analysis User's Manual, 2011.
55. Saito, Y. and M. Yoda, *Fracture toughness and creep crack growth in polypropylene under combined modes I and II loading.* International journal of fracture, 2004. **127**(2): p. L161-L166.
56. Reeder, J.R., *3D mixed-mode delamination fracture criteria–an experimentalist's perspective.* Damage in Composites, 2012. **5**.
57. Richard, H. *Specimens for investigating biaxial fracture and fatigue processes*. in *ICBMFF2*. 2013.
58. Reeder, J., *An Evaluation of Mixed-Mode Delamination Failure Criteria.* 1992.
59. Du, Z.-z., *eXtended Finite Element Method (XFEM) in Abaqus.* 2009.
60. Leung, J.C., et al., *Barbed, Bi-Directional Surgical Sutures*, in *Medical Textiles and Biomaterials for Healthcare*. 2006, Woodhead Publishing. p. 395-403.
61. Ruff, G.L., M.A. Megaro, and J.C. Leung, *Barbed suture in combination with surgical needle*. 2014, Google Patents.
62. Leung, J.C., G.L. Ruff, and M.A. Megaro, *Barb configurations for barbed sutures*. 2016, Google Patents.
63. Shrewsbury, M.M. and K. Kuczynski, *Flexor digitorum superficialis tendon in the fingers of the human hand.* The Hand, 1974. **6**(2): p. 121-133.
64. Ward, S.R., et al., *High stiffness of human digital flexor tendons is suited for precise finger positional control.* Journal of neurophysiology, 2006. **96**(5): p. 2815-2818.
65. Sapienza, A., et al., *Flexor tendon excursion and load during passive and active simulated motion: a cadaver study.* Journal of Hand Surgery (European Volume), 2013. **38**(9): p. 964-971.
66. Edsfeldt, S., et al., *In vivo flexor tendon forces generated during different rehabilitation exercises.* Journal of Hand Surgery (European Volume), 2015. **40**(7): p. 705-710.